


# Pulse Profile Modelling of Thermonuclear Burst Oscillations III : Constraining the properties of XTE J1814-338

Yves Kini<sup>1</sup> , Tuomo Salmi<sup>1</sup>, Serena Vinciguerra<sup>1</sup>, Anna L. Watts<sup>1</sup>, Anna Bilous<sup>2</sup>, Duncan K. Galloway<sup>3</sup>, Emma van der Wateren<sup>4</sup>, Guru Partap Khalsa<sup>1</sup>, Slavko Bogdanov<sup>5</sup>, Johannes Buchner<sup>6</sup>, Valery Suleimanov<sup>7</sup>

<sup>1</sup>*Anton Pannekoek Institute for Astronomy, University of Amsterdam, Science Park 904, 1090GE Amsterdam, the Netherlands*

<sup>2</sup>*Independent researcher*

<sup>3</sup>*School of Physics & Astronomy, Monash University, Clayton, VIC 3800, Australia*

<sup>4</sup>*ASTRON, Netherlands Institute for Radio Astronomy, Oude Hoogeveensedijk 4, 7991 PD, Dwingeloo, The Netherlands*

<sup>5</sup>*Columbia Astrophysics Laboratory, Columbia University, 550 West 120th Street, New York, NY 10027, USA*

<sup>6</sup>*Max Planck Institute for Extraterrestrial Physics, Giessenbachstrasse, 85741 Garching, Germany*

<sup>7</sup>*Institut für Astronomie und Astrophysik, Kepler Center for Astro and Particle Physics, Universität Tübingen, Sand 1, D-72076 Tübingen, Germany*

Accepted XXX. Received YYY; in original form ZZZ

## ABSTRACT

Pulse profile modelling (PPM) is a comprehensive relativistic ray-tracing technique employed to determine the properties of neutron stars. In this study, we apply this technique to the Type I X-ray burster and accretion-powered millisecond pulsar XTE J1814–338, extracting its fundamental properties using PPM of its thermonuclear burst oscillations. Using data from its 2003 outburst, and a single uniform temperature hot spot model, we infer XTE J1814–338 to be located at a distance of  $7.2^{+0.3}_{-0.4}$  kpc, with a mass of  $1.21^{+0.05}_{-0.05}$   $M_{\odot}$  and an equatorial radius of  $7.0^{+0.4}_{-0.4}$  km. Our results also offer insight into the time evolution of the hot spot but point to some potential shortcomings of the single uniform temperature hot spot model. We explore the implications of this result, including what we can learn about thermonuclear burst oscillation mechanisms and the importance of modelling the accretion contribution to the emission during the burst.

**Key words:** dense matter — equation of state — pulsars: general — pulsars: individual (XTE J1814–338) — stars: neutron — X-rays: stars

## 1 INTRODUCTION

Accreting Millisecond X-ray Pulsars (AMXPs) involve a Neutron Star (NS) accreting material, mainly hydrogen and/or helium, from either a degenerate or a non-degenerate star (with mass  $< 1M_{\odot}$ ) through a Roche lobe overflow (Patruno & Watts 2021). The relatively weak magnetic field of the NS in these systems ( $\sim 10^7 - 10^9$  G) leads to the accreted material being channelled to the NS's magnetic poles through an accretion column. The in-falling plasma spreads across the NS's surface, forming a thick plasma shell. With the continuous influx of new material, the previously gathered plasma undergoes hydrostatic compression, leading to significant thermal energy buildup, ultimately culminating in ignition and nuclear burning (see e.g. Bildsten 1998; Keek & Heger 2016, for ignition conditions and burning regime). When the rate of nuclear burning exceeds the cooling rate, a thermonuclear explosion occurs on the surface of the NS. These thermonuclear explosions, commonly referred to

as Type I X-ray bursts, emit intense X-ray radiation (see Galloway et al. 2020; Alizai et al. 2023, for recent reviews).

The discovery of coherent pulsations (Strohmayer et al. 1996), commonly known as thermonuclear burst oscillations, in certain X-ray bursts from specific sources has sparked significant interest in investigating these sources. This interest is motivated not only by the desire to understand the underlying causes of the burst oscillations (see e.g. Spitkovsky et al. 2002; Heyl 2004; Lee 2004; Piro & Bildsten 2005; Cavecchi et al. 2013, 2015, 2016; Mahmoodifar & Strohmayer 2016; Chambers et al. 2019; Garcia et al. 2019; Chambers & Watts 2020; van Baal et al. 2020) but also because these pulsations offer a means to infer important properties of NSs (Bhattacharyya et al. 2005; Lo et al. 2013). In particular, inferring the mass and radius can provide crucial insights into the equation of state for NSs (Lattimer 2012; Oertel et al. 2017; Baym et al. 2018; Tolos & Fabbietti 2020; Yang & Piekarewicz 2020; Hebeler 2021).

Inferring stellar properties using burst oscillations has proven to be complex. This is primarily due to the uncertainties linked to the burning process and oscillation properties, which render modelling of the short time-scale variability associated with the burst

\* E-mail: y.kini@uva.nl

and burst oscillations computationally demanding. [Kini et al. \(2023\)](#) have shown that failing to accurately model these short time-scale variabilities results in biased estimates of mass and radius, particularly for the high number of counts that are needed to derive meaningful constraints on these parameters. To address this bias, bursts can be divided into shorter segments (where variability can be overlooked) while simultaneously fitting the segments ([Kini et al. 2024b](#)). This is referred to as the *slicing method*. [Kini et al. \(2024b\)](#) also verified that posterior distributions of mass and radius, derived from several bursts originating from the same source, can be combined to yield results similar to that of a single burst with an equivalent total number of counts.

[Kini et al. \(2023, 2024b\)](#) employed the Pulse Profile Modelling (PPM) technique, which relies on relativistic ray-tracing. This technique leverages the fact that observed X-ray pulsations carry information about the source’s intrinsic properties (see e.g.: [Pechenick et al. 1983](#); [Chen & Shaham 1989](#); [Page 1995](#); [Miller & Lamb 1998](#); [Braja et al. 2000](#); [Weinberg et al. 2001](#); [Beloborodov 2002](#); [Poutanen & Beloborodov 2006](#); [Cadeau et al. 2007](#); [Morsink et al. 2007](#); [Bauböck et al. 2012](#); [Lo et al. 2013](#); [Psaltis et al. 2014](#); [Miller & Lamb 2015](#); [Stevens et al. 2016](#); [Näätäli & Pihajoki 2018](#); [Bogdanov et al. 2019](#)). Both of our previous studies used the X-ray Pulse Simulation and Inference (X-PSI; [Riley et al. 2023](#)) package, initially developed to model X-ray pulsations from Rotation-Powered Millisecond Pulsars (RMPs) observed by the Neutron Star Interior Composition Explorer (NICER, [Gendreau et al. 2016](#), and see [Riley et al. 2019, 2021](#); [Salmi et al. 2022, 2023](#); [Vinciguerra et al. 2023, 2024](#) for the X-PSI NICER RMP papers). Despite uncertainties about the size, shape, and temperature distribution of the hot spots for RMPs, their pulsations are stable, implying that short-time-scale variability can be overlooked unlike in the case of burst oscillation sources.

To obtain the NS mass and radius, X-PSI computes the expected X-ray pulse profile (phase and spectrally resolved count rate) for a given model and a parameter vector using the PPM technique. X-PSI then compares the expected (model) and observed (data) X-ray pulse profiles by computing the likelihood of the observed X-ray pulse profile given that specific parameter vector and model. Using a Bayesian framework, X-PSI not only derives the posterior probability distributions for space-time parameters (mass and radius) but also for the hot spot properties, which are part of the model.

In [Kini et al. \(2023, 2024b\)](#), we used synthetic data and phenomenological models to mimic the observed bursts and burst oscillation properties from the AMXP XTE J1814–338. This is because XTE J1814–338 was previously identified as one of the most promising sources for PPM ([Bhattacharyya et al. 2005](#)). In this paper, we apply the *slicing method* as in [Kini et al. \(2024b\)](#) to existing observational data of XTE J1814–338 and infer its mass and radius. We also aim to better understand the conditions and the behaviour of the hot spot during the thermonuclear bursts.

The paper is structured as follows. In Section 2, we present the observations, the data reduction, and the instrument models used. This is followed by an explanation of the inference procedures and a summary of the approach we used to combine posterior distributions from multiple bursts to obtain tighter constraints on parameters shared across all bursts. We present the main findings in Section 3, followed by an in-depth discussion of these findings in Section 4. We summarize our conclusions in Section 5.

## 2 MODELLING

In this section, we first provide an overview of the data employed for this analysis and explain the data reduction process. Next, we describe the procedure for extracting the response matrices corresponding to each burst. Finally, we outline the inference approach, focusing on the various model components and the assumptions made to infer the properties of XTE J1814–338.

### 2.1 Burst observations and data reduction

In June of 2003, XTE J1814–338 went into an outburst, the only outburst known to date. Observations with the Rossi X-Ray Timing Explorer (RXTE; [Jahoda et al. 1996](#)) proportional counter arrays at that time resulted in 28 type I X-ray bursts detected over the span of about 50 days ([Strohmayer et al. 2003](#); [Watts et al. 2005](#); [Galloway et al. 2020](#)). The bursts were recorded in Science Event Mode (except for Burst 1), making them suitable for pulse profile modelling. The data for all bursts, except for the first one were acquired with the time resolution of  $2^{-13} \text{ s} \approx 122 \mu\text{s}$  and 64 energy bins spanning the range between 2 and 106 keV (mode E\_125us\_64M\_0\_1s). Burst 1 was captured in GoodXenon mode, with a time resolution of  $1 \mu\text{s}$  and 256 energy bins.

During the observations, four Proportional Counter Units (PCUs) were active. For bursts 5 and 25, PCU0 was excluded from analysis because of abnormally large count rates suggesting a detector breakdown.

The on-burst window was set by the burst count rate surpassing the mean count rate plus five times the standard deviation of the count rate measured in 100-s windows before or after the burst’s occurrence, depending on data availability. Burst start times and durations are given in Table 1.

For the on-burst window, photon arrival times were barycentered with *faxbary* (from the HEASoft package, version 6.28) using spacecraft orbit files and DE405 Solar system ephemerides, with the source coordinates taken from [Papitto et al. \(2007\)](#). The same work provided spin frequency ( $\approx 314.4 \text{ Hz}$ ) and binary ephemerides for computing the spin phase of each photon. The accuracy of the spin phase calculation was verified by visual inspection of the waterfall plot made from the whole dataset. The frequency of burst oscillations is known to fluctuate around the frequency of accretion-powered pulsations used for spin phase calculations ([Cavecchi & Patruno 2022](#)), with the average phase discrepancy reaching 0.04 of spin phase during burst peaks. This is smaller, but comparable to our chosen spin phase bin of 0.0625 (we binned the counts in 16 phase bins).

We generated individual response matrices for each burst using the *pcarsp* tool from the HEASoft package (version 6.28). We used channel subset [1,30], corresponding to the nominal photon energy range [2.06, 12.28] keV for all bursts except Burst 1. For Burst 1, we adjusted the channel subset to [4,30] due to lower counts in the channels below channel 4, corresponding to the nominal photon energy range [2.47, 12.28] keV.

### 2.2 Inference

#### 2.2.1 Models

The models employed to infer XTE J1814–338’s parameters in this work closely resemble those used in [Kini et al. \(2024b\)](#). Here, we outline the key model components and highlight any areas where the approach differs.

In both [Kini et al. \(2024b\)](#) and this paper, we assume the star to be oblate, with the external space-time curvature described by the Schwarzschild metric ([Morsink et al. 2007](#)). After computing the light bending, corrections for relativistic Doppler boosting and aberration are incorporated to account for stellar rotation. We use state-of-the-art neutron star atmospheres developed for thermonuclear burst sources ([Suleimanov et al. 2012](#)), assuming a composition matching solar abundances (as indicated by the burst properties, [Galloway et al. 2008](#)). For interstellar medium (ISM) absorption, we adopt the neutral gas absorption model *Tbabs*, which employs the photoelectric absorption cross-section derived by [Wilms et al. \(2000\)](#). Regarding the X-ray background photons, we make two alternative assumptions described in Section 2.2.2. The likelihood of each sample is computed by marginalization over the background (See Appendix B.2 of [Riley 2019](#), for more details).

To monitor the time evolution of potentially varying parameters throughout each burst, we employ the procedure described in section 2.3 of [Kini et al. \(2024b\)](#). This means that we first divide each burst into 8-time segments and then perform joint modelling of these segments. For this work, we assume that oscillations in each time segment originate from a single circular, uniformly emitting hot spot, as in [Kini et al. \(2024b\)](#). Each hot spot is characterized by its temperature ( $T_{\text{spot}X}$ , with  $X=1, 2, \dots, 8$  the segment's number.), angular radius (or spot size;  $\zeta_{\text{spot}X}$ ), co-latitude ( $\Theta_{\text{spot}X}$ ) and phase shift ( $\phi_{\text{spot}X}$ ). For every burst, we treat  $T_{\text{spot}}$  and  $\zeta_{\text{spot}}$  as free parameters for each segment, without any predetermined order (unlike in [Kini et al. 2024b](#)). We hold the co-latitude and phase shift fixed across all segments of a burst (i.e.  $\Theta_{\text{spot}1} = \Theta_{\text{spot}2} = \dots = \Theta_{\text{spot}8} = \Theta_{\text{spot}}$ , and the same for  $\phi_{\text{spot}X}$ ), but they are expected and allowed to vary from burst to burst. Additionally, we allow the rest of the star to emit with a uniform temperature  $T_{\text{star}}$ . Although  $T_{\text{star}}$  is free to vary between each segment, we impose the trivial constraint ( $T_{\text{spot}X} > T_{\text{star}X}$ ) to expedite the sampling process.

In [Kini et al. \(2024b\)](#) each burst's rise was systematically divided into two segments of 2-seconds each, due to their consistent morphology. In this paper, we take a different approach. The rise is treated as either a single segment or divided in two, with varying time intervals across bursts. This distinction is due to the varying morphology of XTE J1814–338's bursts. Specifically, certain bursts exhibit either a low count rate or a rapid rise, which results in a low number of photons per segment when attempting to partition the burst's onset into two segments. We label the burst morphology as M1 when the rise is treated as one segment and as M2 when the rise is divided into two segments (see Table 1). Due to the uniqueness of each burst, the duration of each segment is not standardized across all bursts, regardless of whether they are M1 bursts or M2 bursts. Each burst is segmented in a manner that ensures minimal variability in flux within each segment. In Figure 1, we present an example of the segmentation process for two bursts exhibiting distinct morphologies. Details on how the remaining bursts are segmented can be found on Zenodo ([Kini et al. 2024a](#)).

In summary, we employ a single hot spot model and segment each burst into 8 time segments to capture the temporal changes of certain parameters. As a result, for a given burst, the final model encompasses 31 free parameters in the sampling space:

- Gravitational mass:  $M$
- Equatorial radius:  $R_{\text{eq}}$
- Source-to-Earth distance:  $D$
- Cosine of the observer's inclination:  $\cos(i)$
- Hot spot co-latitude:  $\Theta_{\text{spot}}$
- Hot spot phase :  $\phi_{\text{spot}}$

Burst	OBSID	Start (days since MJD 52790)	MINBAR ID <sup>*</sup>	Duration (s)	Count	Morphology
1	80138-04-02-00	6.0468	3084	66.60	42736	M2
2	80138-04-03-00	7.2749	3085	106.75	84106	M2
3	80145-02-01-00	7.8899	3086	101.00	82825	M1
4	80418-01-01-01	9.2025	3087	126.99	124670	M2
5	80418-01-01-03	10.1056	3088	90.60	54317	M2
6	80418-01-01-05	11.0356	3089	63.99	35642	M1
7	80418-01-01-08	12.4727	3091	106.75	113816	M2
8	80418-01-01-09	12.5697	3092	75.24	44157	M1
9	80418-01-02-01	13.0658	3093	68.99	58716	M2
10	80418-01-02-00	13.7406	3094	89.74	108361	M2
11	80418-01-02-03	14.0209	3095	102.50	109697	M2
12	80418-01-02-06	15.7959	3096	109.99	115745	M2
13	80418-01-02-07	16.7539	3098	108.74	87581	M2
14	80418-01-02-07	16.8245	3099	44.48	23673	M1
15	80418-01-02-09	17.6734	3100	86.74	110211	M2
16	80418-01-02-04	18.8018	3101	95.24	87928	M2
17	80418-01-02-05	19.7881	3102	88.50	86978	M2
18	80418-01-03-12	20.0747	3103	94.00	111217	M1
19	80418-01-03-00	20.9079	3104	49.73	29630	M2
20	80418-01-03-02	21.6460	3105	111.24	90854	M2
21	80418-01-03-06	22.8951	3106	172.77	101915	M2
22	80418-01-03-07	23.4752	3107	129.60	125149	M2
23	80418-01-04-00	27.7001	3108	79.28	99358	M2
24	80418-01-04-00	27.8898	3109	105.49	90880	M2
25	80418-01-04-01	28.8602	3110	90.56	54317	M2
26	80418-01-05-03	37.2599	3117	119.74	125175	M2
27	80418-01-05-08	38.7997	3118	135.73	97346	M2
28	80418-01-06-07	-	3121	-	-	-

**Table 1.** Burst properties overview. Burst 28 is excluded from this analysis because it shows evidence (although only marginal) of photospheric radius expansion which is not accounted for in our model (see [Strohmayer et al. 2003](#)).

<sup>\*</sup> See [Galloway et al. \(2020\)](#) or <https://burst.sci.monash.edu/>

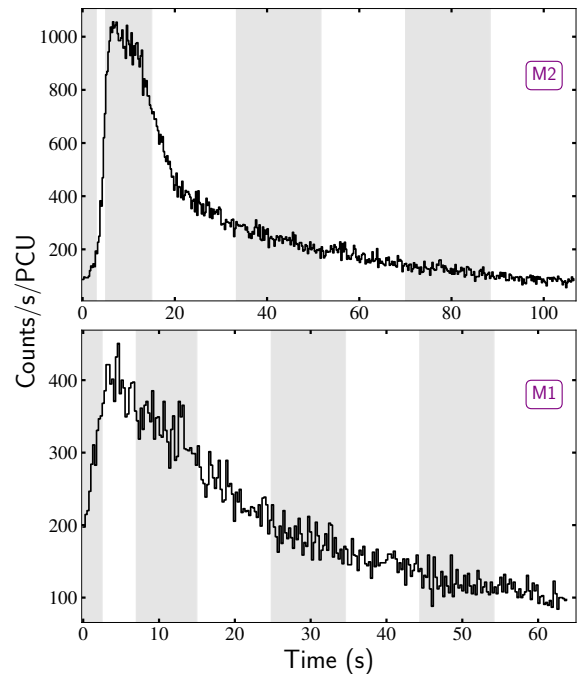


**Figure 1.** Illustrations of M1 and M2 bursts. The M1 burst corresponds to burst 6 of XTE J1814–338, while the M2 burst corresponds to burst 2. These light curves are shown with a time resolution of 0.25 second. The vertical bands denote each individual data segment.

- Interstellar attenuation column density:  $N_H$
- Hot spot temperature (8 in total):  $T_{\text{spot}1}, T_{\text{spot}2}, \dots, T_{\text{spot}8}$
- Hot spot angular radius (8 in total):  $\zeta_{\text{spot}1}, \zeta_{\text{spot}2}, \dots, \zeta_{\text{spot}8}$
- Star temperature (8 in total):  $T_{\text{star}1}, T_{\text{star}2}, \dots, T_{\text{star}8}$

### 2.2.2 Background assumptions

By *background counts* we denote counts unrelated to astronomical sources originating solely from instrumental noise (instrumental background), as well as counts from other sources in the field of view, along with any additional sources of unpulsed emission from the X-ray binary itself. In PPM, the background model can significantly influence the inferred properties of the NS (see e.g. [Salmi et al. 2022](#), for an in-depth discussion). Since the background model and counts during a burst are not well constrained, in this analysis, we employed two approaches.

In the `Bkg free` case, we refrained from imposing a specific model for the background, allowing it to vary freely as a parameter for each RXTE instrument channel. In the `Bkg constrained` case, we assumed that during the burst, the upper limit of the background exhibits the same spectrum as the pre-burst emission. Recognizing that bursts are expected to disrupt the accretion flow, resulting in temporal variations in background counts throughout the burst ([Worpel et al. 2015](#)), we set the lower limit of the background to 0 and the upper limit to the pre-burst counts times a scaling factor,  $f_a$ , which represents the persistent model normalization as defined in [Worpel et al. \(2015\)](#). To compute  $f_a$  for each time segment, we used the average upper limit obtained from a previous XTE J1814–338 spectrum analysis ([Worpel et al. 2015](#)). For the pre-burst level, we took the first 10s before the start of each burst.

### 2.2.3 Higher-order images

For sufficiently compact stars, photons originating from the same point on the stellar surface can reach the observer via multiple trajectories. Thus, higher-order images are expected for  $R_{\text{pole}}c^2/GM < 3.52$  (see [Bogdanov et al. 2021](#), and references therein) where  $R_{\text{pole}}$  is the polar radius. During the inference runs in the `Bkg free` case, we imposed no restrictions on the image order. Images are summed over until higher-order images are no longer visible. This is computationally expensive, particularly when exploring regions of high compactness. Hence, in the `Bkg constrained` case (for which computational cost turned out to be much higher), we conducted the inference runs without imposing any restrictions on the image order only for the first ten bursts. Due to computational limitations, we set the image order to 1 for the remaining bursts. This implies that only the primary image is computed. For Burst 1 we ran both and confirmed that the choice did not affect the results.

### 2.2.4 Posterior computation

Given the model (which incorporates the relativistic ray-tracing, ISM, atmosphere, hot spot properties, and instrument response), we explore the parameter space and gauge how probable parameters ( $\theta = (M, R_{\text{eq}}, D, \cos(i), \phi_{\text{spot}}, \Theta_{\text{spot}}, \zeta_{\text{spot}1}, \dots, \zeta_{\text{spot}8}, T_{\text{spot}1}, \dots, T_{\text{spot}8}, T_{\text{star}1}, \dots, T_{\text{star}8}, N_H)$ ) are, based on both prior beliefs (see Section 2.2.5) and the new evidence provided by the burst data. We employ Bayes' formalism:

$$p(\theta_i|d_i) = \frac{p(d_i|\theta_i)p(\theta_i)}{p(d_i)}, \quad (1)$$

where  $\theta_i$  is a model parameter vector for the  $i^{\text{th}}$  burst,  $d_i$  the corresponding data.  $p(\theta_i|d_i)$  the posterior probability of the parameters  $\theta_i$  given the data  $d_i$ ,  $p(d_i|\theta_i)$  the likelihood of observing the data  $d_i$  given the parameters  $\theta_i$ ,  $p(\theta_i)$  the prior probability (or initial belief about  $\theta_i$ ), and  $p(d_i)$  the evidence.

Ideally, conducting a comprehensive joint inference run involving all the bursts, while keeping parameters such as  $M, R_{\text{eq}}, D, \cos(i), N_H$  fixed across the bursts, with the remaining parameters allowed to vary within and across bursts, would be preferred. However, with 27 bursts for XTE J1814–338, this would entail exploring a parameter space with 707 dimensions, which is computationally challenging using current Nested Sampling techniques. In practice, we compute the posterior probability of the  $N$  bursts, using X-PSI<sup>1</sup> version v2.0.0. Within X-PSI, this process is carried out using MultiNest ([Feroz & Hobson 2008](#); [Feroz et al. 2009, 2019](#)) coupled with PyMultiNest ([Buchner et al. 2014](#)). Although certain parameters (like mass) will be the same for all bursts, we compute the posterior probability of each sampled parameter vector for each burst independently. We do this for the sake of computational efficiency. The resulting posteriors from the  $N$  bursts are then combined to derive the main results presented in this paper.

To combine these posteriors, we follow the methodology outlined in section 2.4 of [Kini et al. \(2024b\)](#). We compute the combined posterior probability of a common set of parameters  $\alpha$  using Equation 5 of [Kini et al. \(2024b\)](#):

$$p(\alpha|\mathcal{D}) \propto \prod_{i=1}^N p(\alpha|d_i), \quad (2)$$

where  $d_i$  is the data corresponding to the  $i^{\text{th}}$  burst,  $\mathcal{D} = \{d_i\}_{i=1}^N$  the set of data corresponding to the  $N$  bursts,  $p(\alpha|d_i)$  the posterior of the parameters  $\alpha$  given the data  $d_i$ , and  $p(\alpha|\mathcal{D})$  the combined posterior of the parameters  $\alpha$  given the  $N$  bursts.

To combine the posterior distributions using Equation 2, [Kini et al. \(2024b\)](#) employed a mesh featuring 400 points for each element of  $\alpha$  (where  $\alpha = (M, R_{\text{eq}})^2$ ). However, using this grid resolution for  $\alpha = (M, R_{\text{eq}}, D, \cos(i), N_H)$  would entail computing the posteriors for 400<sup>5</sup> points, rendering it computationally impractical. Alternatively, one could set  $\alpha = (M, R_{\text{eq}})$  and marginalize over the remaining parameters. Yet, this approach carries the risk of overlooking correlations between  $M$ ,  $R$ , and the marginalized parameters<sup>3</sup>.

Hence, instead of relying on the grid method, we initially approximate  $p(\alpha|d_i)$  using Gaussian Kernel Density Estimation (KDE) from `scipy` ([Virtanen et al. 2020](#)). Unlike in [Kini et al. \(2024b\)](#), where the KDE bandwidth was fixed at a specific value ( $\text{bw}=0.1$ ) to estimate  $p(\alpha|d_i)$ , here we adopt Scott's rule of thumb from `scipy` ([Scott 1992](#)). This rule dynamically calculates the appropriate bandwidth for the KDE for each of the  $N$  bursts, considering both the sample size and the data variance. Then, we define

<sup>1</sup> <https://github.com/xpsi-group/xpsi>

<sup>2</sup> Some of the remaining parameters were assumed to be well constrained a priori.

<sup>3</sup> Footnote 11 of [Kini et al. \(2024b\)](#) only applies if there are no correlations between parameters or if the correlations are the same.



a new likelihood function,  $\mathcal{L} \propto \prod_{i=1}^N p(\alpha|d_i)$ , with  $p(\alpha|d_i)$  representing the probability density function obtained using `scipy`. We sample the prior space of  $\alpha$  using the new likelihood to derive the posterior distributions of  $\alpha$  using `MultiNest` and `PyMultiNest`.

We also checked that when setting  $\alpha = (M, R_{\text{eq}}, D)$ , both the grid method and the sampling method yielded similar results, as a check of our new sampling approach. However, the computational costs are drastically different: about  $5 \times 10^4$  core hours for the grid method and 60 core hours for the sampling method.

In Table A2 of Appendix A, we present the sampler settings used to explore the prior space during inference for each burst. Additionally, we detail the settings employed when combining bursts. When combining bursts, we explored the joint  $(M, R_{\text{eq}}, D, \cos(i), N_H)$  parameter space using two distinct settings. Initially, we conducted explorations with  $2 \times 10^3$  live points, followed by another round with  $10^5$  live points. Both settings yielded similar outcomes (see Figure A3 in Appendix A).

### 2.2.5 Prior choice

For XTE J1814–338, prior knowledge of the parameters of interest is not as robust as that seen in some of the RMP sources examined using PPM (see e.g. Riley et al. 2021; Salmi et al. 2022). Consequently, we opt for a broad prior distribution for the majority of these parameters:  $M, R_{\text{eq}}, \cos(i), \phi_{\text{spot}}, \Theta_{\text{spot}}, \zeta_{\text{spot}1}, \dots, \zeta_{\text{spot}8}, T_{\text{spot}1}, \dots, T_{\text{spot}8}, T_{\text{star}1}, \dots, T_{\text{star}8}, N_H$ . These prior choices are summarized in Table 2. We also apply implicit prior criteria described in greater detail in section 2.5 of Kini et al. (2023) to expedite parameter sampling. These implicit prior criteria are summarized as follows:

- We discard samples with  $R_{\text{pole}}/r_g(M) < 2.9$  to ensure compliance with the causality limit (see e.g. Gandolfi et al. 2012).  $R_{\text{pole}}$  is the polar radius and  $r_g(M) = GM/c^2$ .
- Samples with  $\log g \notin [13.7, 14.9]$  are rejected to align with the range of surface gravities defined within the atmosphere table.

For distance, the situation is complicated. There is no Gaia distance for this source (Gaia Collaboration et al. 2016). A study of the optical counterpart in quiescence, by Baglio et al. (2013), suggests a distance  $\sim 11$  kpc but this is also quite uncertain and is calculated assuming a NS mass of  $1.4 M_{\odot}$ . Another estimate can be obtained from the marginal detection of PRE in the brightest burst from this source (Burst 28) (Strohmayer et al. 2003). If the peak luminosity of the brightest burst can indeed be equated with the Eddington limit then the distance is given by (see Galloway et al. 2008):

$$d = 8.6 \left( \frac{F_{\text{peak}}}{3 \times 10^{-8} \text{erg cm}^{-2} \text{s}^{-1}} \right)^{-1/2} \left( \frac{M}{1.4 M_{\odot}} \right)^{1/2} \times \left( \frac{1 + z(M, R)}{1.31} \right)^{-1/2} (1 + X)^{-1/2} \text{ kpc} \quad (3)$$

where  $F_{\text{peak}}$  is the peak flux of the PRE burst,  $M$  the NS mass,  $R$  ( $R \approx R_{\text{eq}}$ ) the NS radius,  $1 + z(M, R) = (1 - 2GM/Rc^2)^{-1/2}$  the gravitational redshift, and  $X$  the hydrogen mass fraction.

For a marginal detection of PRE, where the peak flux of the brightest burst might not reach the Eddington limit, this yields instead an upper limit on distance. Considering the bounds of the prior distribution for both mass and radius and under the assumption of the extreme scenario where burst 28 exclusively involves pure Helium burning ( $X=0.0$ ), we have determined an estimated distance

**Table 2.** Parameters and their respective prior density used for sampling.

Parameter	Prior density
$M (M_{\odot})$	$M \sim \mathcal{U}(1.0, 3.0)$
$R_{\text{eq}} (\text{km})$	$R_{\text{eq}} \sim \mathcal{U}(3r_g(1.0), 16.0)^{\star}$
$D (\text{kpc})$	$D \sim \mathcal{U}(3.0, 14.0)$
$\cos(i)$	$\cos(i) \sim \mathcal{U}(0.0, 1.0)$
$\phi_{\text{spot}} (\text{cycles})$	$\phi_{\text{spot}} \sim \mathcal{U}(-0.25, 0.75)$
$\Theta_{\text{spot}} (\text{radian})$	$\cos(\Theta_{\text{spot}}) \sim \mathcal{U}(-1.0, 1.0)$
$\zeta_{\text{spotX}} (\text{rad})$	$\zeta_{\text{spot}} \sim \mathcal{U}(0.0, \pi/2)$
$\log[T_{\text{spotX}} (\text{K})/1\text{K}]$	$\log[T_{\text{spot}} (\text{K})/1\text{K}] \sim \mathcal{U}(6.7, 7.6)^{\dagger}$
$\log[T_{\text{starX}} (\text{K})/1\text{K}]$	$\log[T_{\text{star}} (\text{K})/1\text{K}] \sim \mathcal{U}(6.7, 7.6)$
$N_H (10^{20} \text{cm}^{-2})$	$N_H \sim \mathcal{U}(9.0, 100.0)$

$\star$   $r_g(1.0)$ : Solar Schwarzschild gravitational radius.

$\dagger$  Temperature bounds set by bursting atmosphere table computed as described in more detail in Kini et al. (see 2023).

of approximately 14 kpc. Hence, we chose this as an upper limit for the distance. For the lower bounds for the distance, we opt for 3 kpc. This is motivated by the expectation that XTE J1814–338 is likely to be located no closer than 3.8 kpc (Krauss et al. 2005). This lower limit on the distance was obtained by fitting the phase-averaged X-ray spectrum of XTE J1814–338 in outburst.

## 3 RESULTS

We conducted a total of 54 inference runs, with 27 each for both the Bkg free and Bkg constrained cases. Of these, 53 runs were completed successfully. However, Burst 23 in the Bkg constrained case had to be halted due to excessive computational demand. Imposing a constraint on the background during inference mostly leads to a significantly higher number of likelihood evaluations before the run converges, resulting in longer run times. Therefore, the results for the combined bursts do not include Burst 23 for either of the cases. The total number of counts excluding Burst 23 is 2197642. The total computing time is about 2.4 million and 4.8 million core hours (excluding burst 23 run time) respectively for the Bkg free and Bkg constrained cases. The details of runtimes for each burst are highlighted in Table A1 of Appendix A.

In this section, we first assess the one-hot-spot model quality in Section 3.1. Starting from Section 3.2, we highlight the properties of XTE J1814–338 along with the characteristics of the bursts and oscillations that we obtain from PPM. We first cover the parameters known to be common to all bursts: mass, radius, distance, observer inclination, and column density. Then we present the findings for the parameters that vary with time during the burst and from burst to burst.

### 3.1 Model quality

In Figure 2, we present the residual plots for Burst 1 for both the Bkg free and Bkg constrained cases for the first three segments. These residuals are computed using the maximum likelihood solution in each case. Residuals for the remaining segments and bursts are available on Zenodo (see Kini et al. 2024a). We also show the distribution of the residuals for Burst 1 in Figure A1 of Appendix

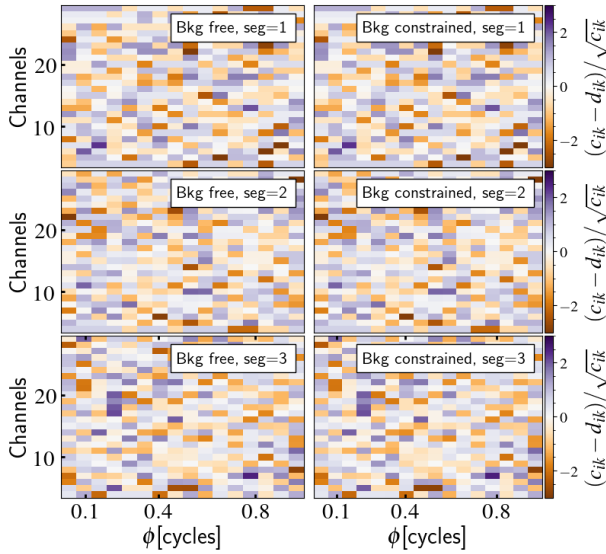


**Figure 2.** Residual plots for Burst 1 for the first three segments for Bkg free (left) and Bkg constrained (right). The residuals are the difference between the model counts (for the maximum likelihood solution) and the data counts, normalized by the model count counts in each instrument energy channel and phase bin.  $c_{ik}$  and  $d_{ik}$  denote respectively the model counts and the data counts in the  $i^{th}$  rotation phase and  $k^{th}$  energy channel.

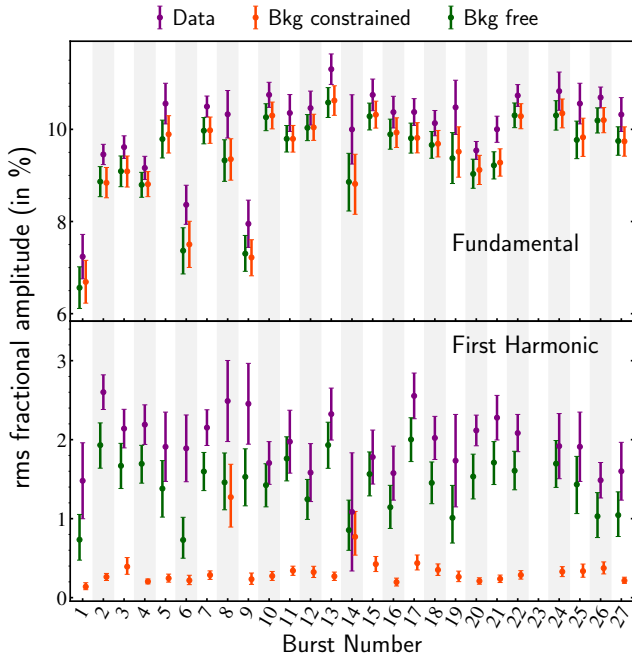


**Figure 3.** Medians and 68% credible intervals of the probability distribution of the bolometric (combined across segments) rms FA of the single hot spot model for both the fundamental (top) and the first harmonic (bottom) in each burst in the Bkg free and Bkg constrained cases alongside rms FA in the data.

A. Notably, none of the residuals reveal discernible patterns or clustering, or a deviation from the overall expected distribution, either of which might suggest that the model’s performance is inadequate. However, evaluating the model quality solely based on residuals may not provide a complete assessment.

Comparing the medians (and 68% credible intervals) of the probability distribution of the bolometric (combined across segments) root mean square fractional amplitude (rms FA) from the (single hot spot) model for both the fundamental and the first harmonic to that of the data, as illustrated in Fig 3, reveals interesting insights. Across both the Bkg free and Bkg constrained cases, the rms FAs of the fundamental are almost all consistent, within 68% credible intervals, with the rms FAs observed in the data. This suggests that the model can reproduce the rms FA of the fundamental in the data. However, it is notable the rms FAs in both Bkg free and Bkg constrained cases are consistently lower than those observed in the data. A similar trend is observable in the Bkg free case for the second harmonic for most bursts. However, for the first harmonic, in the Bkg constrained case, rms FAs are significantly lower than the values observed in the data. The rms FA of all the bursts, except from Burst 14, cannot reproduce the rms FA observed in the data. These suggest that the single hot spot model, particularly under the Bkg constrained scenario, struggles to accurately model the data.

### 3.2 Common parameters shared across all bursts

In Table 3, we show the inferred values of the mass, radius, distance, observer’s inclination, and column density for each burst for both the Bkg free and the Bkg constrained cases. The table also shows the combined result in the last row. The provided values are the median of the posterior distribution and the 68% credible interval. These values are derived using the samples and their corresponding posteriors obtained through the method described in Section 2.2.4. The complete posterior plots for each burst can be accessed on Zenodo (see [Kini et al. 2024a](#)). We found that, for the initial runs where we leave the background free (Bkg free), the average uncertainties of the upper (lower) 68% credible interval for the mass and radius, for a single burst are +26%(−19%) and +18%(−16%) respectively. For the Bkg constrained case, the average uncertainties are +26%(−12%) and +22%(−22%) respectively for the mass and radius. The results also show that constraining the background systematically leads to smaller distances and inclinations compared to when the background is left unconstrained.

In Figure 4, we present the combined posterior distribution plots of the common parameters, using information from the 26 bursts. The combined posteriors for each subset (M1 and M2) are shown in Figure A2 of Appendix A. The two-dimensional posterior distributions are, from most opaque to least, the 68%, 95%, and 99% posterior credible region. The solid (dash-dotted) lines in the 1D credible interval panels represent each parameter’s marginalized posterior (prior) distribution. The vertical bands are the inferred 68% credible intervals.

A prominent observation is the emergence of a multimodal likelihood surface. While 3 modes were identified using  $2 \times 10^3$  live points, this number increased to 9 when employing  $10^5$  live points. However, irrespective of the sampler settings, the preferred solution remains consistent based on the evidence (Table A3 of the Appendix A for an overview of the Maximum A Posteriori (MAP) for each mode). In this section, we present the posterior distributions obtained using  $2 \times 10^3$  live points.

For the scenario with unconstrained background, the inferred

values for mass, radius, and distance are  $1.36^{+0.07}_{-0.07} M_{\odot}$ ,  $9.9^{+0.4}_{-0.4}$  km, and  $12.2^{+0.4}_{-0.5}$  kpc, respectively. The uncertainties (the full 68% credible interval) associated with mass and radius are approximately  $\Delta M/M \approx 10\%$  and  $\Delta R_{\text{eq}}/R_{\text{eq}} = 8\%$ , respectively. The corresponding values for  $\cos(i)$  and  $N_H$  are  $0.16^{+0.05}_{-0.04}$  and  $26.9^{+5.3}_{-4.4} \times 10^{20} \text{ cm}^{-2}$ . The overall inferred background is very high, for more discussion see Section 4.1.1.

Conversely, under the constraint of an upper limit on the background (Bkg constrained), the inferred parameters adjust to  $1.21^{+0.05}_{-0.05} M_{\odot}$  for mass,  $7.0^{+0.4}_{-0.4}$  km for radius, and  $7.2^{+0.3}_{-0.4}$  kpc for distance. This time, the uncertainties in mass and radius are approximately  $\Delta M/M \approx 8\%$  and  $\Delta R_{\text{eq}}/R_{\text{eq}} = 11\%$ . The inferred values for  $\cos(i)$  and  $N_H$  become  $0.84^{+0.01}_{-0.01}$  and  $27.84^{+6.72}_{-4.34} \times 10^{20} \text{ cm}^{-2}$ , respectively.

While the combined estimations of the mass, and  $N_H$  do not exhibit inconsistency between the Bkg free and Bkg constrained cases, notable disparities emerge in the inferred values for radius, distance, and  $\cos(i)$ . In the Bkg constrained case, we inferred a lower radius and distance and a smaller observer inclination.

### 3.3 Burst and burst oscillation properties

Given that the origins of the burst oscillations and the burning characteristics are not known a priori, we assume the hot spot temperature, angular radius, and stellar temperature are free parameters that can vary across segments, as mentioned in Section 2.2.1. By adopting this approach, we aim to capture the variations in these parameters, which could offer insights into the poorly understood physics underlying the burst and oscillation properties. In Figure 5, we present the time evolution of the hot spot temperature, angular radius and stellar temperature or both the Bkg free and the Bkg constrained case. We plot the inferred medians, along with the 68% credible intervals for each morphology (M1 and M2).

The models employed for inference allow for the possibility of the hot spot size and temperature as well as the rest of the star temperature to change throughout the burst, while the position of the hot spot remains fixed. This flexibility leads to a multitude of potential permutations. However, the results of the inference runs indicate a clear preference for a particular solution: one where the stellar temperature remains constant during the bursts, while the temperature and size of the hot spot vary. The stellar temperature is mostly consistent with being constant at the  $1\sigma$  level whereas the hot spot temperature and size are not, especially in the Bkg constrained case.

Despite fluctuations in the hot spot temperature observed during the burst in the Bkg free scenario, it is evident that in that case the overall burst light curve is mostly determined by the changes in the background, as illustrated in Figure 6. Figure 6 shows an example (for Burst 1, see Zenodo, Kini et al. 2024a for the remaining bursts) of the contribution from the hot spot, the star, and the background to the overall burst as a function of time. Both the hot spot and stellar contributions to the overall counts are negligible. While a dominating background solution is favored in Bkg free, it likely does not accurately reflect the true nature of a burst, as we discuss in Section 4. Conversely, in the Bkg constrained case, the primary factors influencing the overall burst light curve are the variations in hot spot temperature and size, with the exception of five bursts (Bursts 1,6,8,9,14) where the background contribution remains high (see Zenodo Kini et al. 2024a). For these bursts this is due to a high background limit derived from elevated pre-burst levels (see Section 2.2.2).

Both the Bkg free and Bkg constrained scenarios exhibit a preference for a large hot spot size. In the Bkg free case, the hot spots tend to be located away from the poles, typically in the vicinity of the equator. Conversely, in the Bkg constrained scenario, the hot spots are mostly located roughly halfway between the equator and the stellar northern rotational pole, as illustrated in Figure 7. Figure 7 shows the median and the 68% credible interval of the co-latitude of the centre of the hot spot for each burst for both the Bkg free and the Bkg constrained cases. The co-latitude of the centre of the hot spot for burst 8 and burst 14 is similar in both cases because they have particularly high inferred backgrounds.

## 4 DISCUSSION

### 4.1 Common parameters

#### 4.1.1 Initial runs: Bkg free case

The inferred background in the Bkg free case is very high, dominating the overall burst count rate, while the contribution from the spot and the stellar component is almost negligible (see Figure 6). Such a scenario is inconsistent with current Type I X-ray burst models, where bursts arise from unstable thermonuclear burning of accreted fuel on the surface of neutron stars (e.g. Hansen & van Horn 1975), rather than simply from an increase in the persistent emission from the accretion disk/column.

The inferred distance for the Bkg free case is very large,  $12.2^{+0.4}_{-0.5}$  kpc. It is, however, consistent with the distance inferred by Baglio et al. (2013) (see Figure 8). Leveraging data obtained from the European Southern Observatory Very Large Telescope, Baglio et al. (2013) conducted an analysis of the quiescent optical counterpart of XTE J1814–338, using multiband orbital phase-resolved photometry. Employing the Markov Chain Monte Carlo method to analyze and model the light curves, they constrained the distance to XTE J1814–338. Assuming a neutron star mass of  $1.4 M_{\odot}$ , which is close to the inferred mass of XTE J1814–338 in the Bkg free scenario, they arrived at a distance modulus of 15.2, equivalent to an estimated distance of approximately 11 kpc. However, the inferred distance in the Bkg free scenario does not align with the upper limit of 9.6 kpc deduced by Strohmayer et al. (2003).

Strohmayer et al. (2003) assumed a canonical star (similar to our mass and radius findings), with a hydrogen-rich photosphere, and used the peak luminosity of Burst 28 as the Eddington luminosity. When computing this upper limit, certain considerations, such as burst anisotropy, were not taken into account in their approach. To investigate how factors such as anisotropy and fuel composition impact the distance estimate, we employed a recently developed code Concord (Galloway et al. 2022). Concord<sup>4</sup> offers a comprehensive approach to estimating Type I X-ray burster system parameters such as the distance while fully accounting for astrophysical uncertainties. In Figure 8, we present the expected distance distributions across various atmospheric compositions. These distributions are derived from the medians of the masses and radii and observer inclination distributions obtained under both the Bkg free and Bkg constrained cases. The distance inferred in the Bkg free case is inconsistent with the distance distributions when considering Burst 28 as a PRE burst with the mass, radius, and inclination that we infer for this case.

<sup>4</sup> <https://github.com/outsider/concord>

Burst	$M (M_{\odot})$		$R_{\text{eq}} \text{ (km)}$		$D \text{ (kpc)}$		$\cos(i)$		$N_H (10^{20} \text{cm}^{-2})$	
	Bkg free	Bkg con	Bkg free	Bkg con	Bkg free	Bkg con	Bkg free	Bkg con	Bkg free	Bkg con
1	1.52 <sup>+0.47</sup> <sub>-0.33</sub>	1.57 <sup>+0.48</sup> <sub>-0.36</sub>	10.06 <sup>+2.23</sup> <sub>-2.03</sub>	11.42 <sup>+2.55</sup> <sub>-2.70</sub>	10.95 <sup>+1.89</sup> <sub>-2.16</sub>	9.85 <sup>+2.00</sup> <sub>-2.05</sub>	0.35 <sup>+0.26</sup> <sub>-0.22</sub>	0.86 <sup>+0.07</sup> <sub>-0.13</sub>	50.51 <sup>+29.19</sup> <sub>-26.23</sub>	44.56 <sup>+30.11</sup> <sub>-23.04</sub>
2	1.36 <sup>+0.36</sup> <sub>-0.23</sub>	1.73 <sup>+0.46</sup> <sub>-0.39</sub>	10.93 <sup>+1.77</sup> <sub>-1.57</sub>	11.01 <sup>+2.32</sup> <sub>-2.58</sub>	12.41 <sup>+1.07</sup> <sub>-1.61</sub>	10.65 <sup>+1.80</sup> <sub>-2.05</sub>	0.26 <sup>+0.21</sup> <sub>-0.16</sub>	0.83 <sup>+0.08</sup> <sub>-0.13</sub>	45.26 <sup>+31.25</sup> <sub>-23.95</sub>	44.81 <sup>+30.11</sup> <sub>-23.26</sub>
3	1.33 <sup>+0.34</sup> <sub>-0.22</sub>	1.37 <sup>+0.39</sup> <sub>-0.24</sub>	10.69 <sup>+1.83</sup> <sub>-1.65</sub>	9.39 <sup>+2.73</sup> <sub>-2.23</sub>	11.92 <sup>+1.38</sup> <sub>-1.93</sub>	9.88 <sup>+2.06</sup> <sub>-1.75</sub>	0.28 <sup>+0.23</sup> <sub>-0.18</sub>	0.74 <sup>+0.13</sup> <sub>-0.23</sub>	42.75 <sup>+31.93</sup> <sub>-22.81</sub>	36.14 <sup>+29.65</sup> <sub>-18.02</sub>
4	1.65 <sup>+0.40</sup> <sub>-0.35</sub>	1.83 <sup>+0.37</sup> <sub>-0.39</sub>	12.06 <sup>+1.74</sup> <sub>-1.74</sub>	13.54 <sup>+1.57</sup> <sub>-2.23</sub>	12.49 <sup>+1.03</sup> <sub>-1.59</sub>	10.42 <sup>+1.03</sup> <sub>-1.47</sub>	0.24 <sup>+0.19</sup> <sub>-0.15</sub>	0.86 <sup>+0.05</sup> <sub>-0.08</sub>	47.77 <sup>+31.25</sup> <sub>-25.54</sub>	54.39 <sup>+28.05</sup> <sub>-28.28</sub>
5	1.40 <sup>+0.34</sup> <sub>-0.25</sub>	1.40 <sup>+0.31</sup> <sub>-0.24</sub>	9.48 <sup>+1.68</sup> <sub>-1.48</sub>	8.95 <sup>+1.88</sup> <sub>-1.97</sub>	12.37 <sup>+1.10</sup> <sub>-1.66</sub>	11.01 <sup>+1.79</sup> <sub>-1.94</sub>	0.28 <sup>+0.23</sup> <sub>-0.18</sub>	0.77 <sup>+0.10</sup> <sub>-0.16</sub>	51.19 <sup>+30.11</sup> <sub>-27.37</sub>	63.51 <sup>+23.95</sup> <sub>-31.47</sub>
6	1.76 <sup>+0.50</sup> <sub>-0.42</sub>	1.74 <sup>+0.54</sup> <sub>-0.43</sub>	10.26 <sup>+2.41</sup> <sub>-2.12</sub>	9.42 <sup>+2.46</sup> <sub>-2.35</sub>	11.83 <sup>+1.44</sup> <sub>-2.04</sub>	10.25 <sup>+2.22</sup> <sub>-2.34</sub>	0.39 <sup>+0.26</sup> <sub>-0.24</sub>	0.76 <sup>+0.14</sup> <sub>-0.25</sub>	52.33 <sup>+29.65</sup> <sub>-27.60</sub>	50.28 <sup>+30.56</sup> <sub>-26.46</sub>
7	1.70 <sup>+0.37</sup> <sub>-0.35</sub>	1.66 <sup>+0.45</sup> <sub>-0.38</sub>	11.45 <sup>+1.71</sup> <sub>-1.77</sub>	11.59 <sup>+2.55</sup> <sub>-2.73</sub>	12.07 <sup>+1.30</sup> <sub>-1.83</sub>	9.34 <sup>+1.73</sup> <sub>-1.90</sub>	0.25 <sup>+0.21</sup> <sub>-0.16</sub>	0.83 <sup>+0.08</sup> <sub>-0.13</sub>	42.98 <sup>+31.70</sup> <sub>-22.81</sub>	44.81 <sup>+31.47</sup> <sub>-23.72</sub>
8	1.42 <sup>+0.41</sup> <sub>-0.27</sub>	1.41 <sup>+0.38</sup> <sub>-0.26</sub>	10.03 <sup>+2.06</sup> <sub>-1.77</sub>	10.06 <sup>+2.09</sup> <sub>-1.86</sub>	11.74 <sup>+1.48</sup> <sub>-1.99</sub>	11.72 <sup>+1.48</sup> <sub>-1.94</sub>	0.30 <sup>+0.25</sup> <sub>-0.19</sub>	0.32 <sup>+0.25</sup> <sub>-0.21</sub>	46.40 <sup>+31.25</sup> <sub>-24.86</sub>	46.40 <sup>+31.25</sup> <sub>-24.86</sub>
9	1.49 <sup>+0.57</sup> <sub>-0.33</sub>	1.85 <sup>+0.37</sup> <sub>-0.41</sub>	12.20 <sup>+2.03</sup> <sub>-2.06</sub>	11.56 <sup>+1.97</sup> <sub>-2.73</sub>	12.20 <sup>+1.20</sup> <sub>-1.84</sub>	11.86 <sup>+1.43</sup> <sub>-2.29</sub>	0.26 <sup>+0.22</sup> <sub>-0.17</sub>	0.77 <sup>+0.11</sup> <sub>-0.16</sub>	49.82 <sup>+30.33</sup> <sub>-26.46</sub>	49.37 <sup>+30.33</sup> <sub>-26.00</sub>
10	1.48 <sup>+0.36</sup> <sub>-0.29</sub>	1.41 <sup>+0.40</sup> <sub>-0.26</sub>	11.07 <sup>+1.83</sup> <sub>-1.94</sub>	10.90 <sup>+2.61</sup> <sub>-2.44</sub>	11.49 <sup>+1.59</sup> <sub>-1.97</sub>	8.84 <sup>+1.74</sup> <sub>-1.63</sub>	0.30 <sup>+0.23</sup> <sub>-0.19</sub>	0.82 <sup>+0.09</sup> <sub>-0.15</sub>	43.67 <sup>+31.93</sup> <sub>-23.26</sub>	41.84 <sup>+31.25</sup> <sub>-21.89</sub>
11	1.38 <sup>+0.33</sup> <sub>-0.24</sub>	1.96 <sup>+0.45</sup> <sub>-0.45</sub>	11.30 <sup>+1.74</sup> <sub>-1.59</sub>	13.80 <sup>+1.45</sup> <sub>-2.29</sub>	12.36 <sup>+1.10</sup> <sub>-1.67</sub>	11.29 <sup>+1.22</sup> <sub>-1.57</sub>	0.27 <sup>+0.23</sup> <sub>-0.18</sub>	0.81 <sup>+0.08</sup> <sub>-0.11</sub>	41.16 <sup>+31.70</sup> <sub>-21.89</sub>	39.79 <sup>+31.47</sup> <sub>-20.98</sub>
12	1.24 <sup>+0.26</sup> <sub>-0.16</sub>	1.29 <sup>+0.33</sup> <sub>-0.19</sub>	9.45 <sup>+1.74</sup> <sub>-1.59</sub>	9.39 <sup>+2.78</sup> <sub>-2.12</sub>	11.00 <sup>+1.83</sup> <sub>-2.03</sub>	8.56 <sup>+2.03</sup> <sub>-1.72</sub>	0.33 <sup>+0.25</sup> <sub>-0.21</sub>	0.79 <sup>+0.09</sup> <sub>-0.16</sub>	40.70 <sup>+31.70</sup> <sub>-21.44</sub>	39.11 <sup>+30.79</sup> <sub>-20.30</sub>
13	1.36 <sup>+0.32</sup> <sub>-0.23</sub>	1.23 <sup>+0.26</sup> <sub>-0.15</sub>	10.75 <sup>+1.74</sup> <sub>-1.65</sub>	8.81 <sup>+2.12</sup> <sub>-1.74</sub>	11.72 <sup>+1.47</sup> <sub>-1.91</sub>	9.16 <sup>+1.74</sup> <sub>-1.54</sub>	0.25 <sup>+0.21</sup> <sub>-0.16</sub>	0.80 <sup>+0.10</sup> <sub>-0.17</sub>	37.51 <sup>+30.79</sup> <sub>-19.39</sub>	31.81 <sup>+26.68</sup> <sub>-15.51</sub>
14	1.52 <sup>+0.45</sup> <sub>-0.32</sub>	1.56 <sup>+0.45</sup> <sub>-0.33</sub>	8.58 <sup>+2.17</sup> <sub>-1.80</sub>	8.37 <sup>+2.17</sup> <sub>-1.80</sub>	11.14 <sup>+1.85</sup> <sub>-2.56</sub>	10.96 <sup>+1.95</sup> <sub>-2.57</sub>	0.32 <sup>+0.26</sup> <sub>-0.21</sub>	0.34 <sup>+0.27</sup> <sub>-0.22</sub>	49.60 <sup>+29.88</sup> <sub>-26.23</sub>	49.82 <sup>+30.11</sup> <sub>-26.46</sub>
15	1.44 <sup>+0.37</sup> <sub>-0.28</sub>	1.59 <sup>+0.47</sup> <sub>-0.36</sub>	11.30 <sup>+1.91</sup> <sub>-1.86</sub>	12.26 <sup>+2.26</sup> <sub>-2.81</sub>	11.86 <sup>+1.41</sup> <sub>-1.86</sub>	10.41 <sup>+1.69</sup> <sub>-2.05</sub>	0.31 <sup>+0.24</sup> <sub>-0.20</sub>	0.78 <sup>+0.10</sup> <sub>-0.15</sub>	45.04 <sup>+31.70</sup> <sub>-23.95</sub>	42.98 <sup>+31.70</sup> <sub>-22.81</sub>
16	1.23 <sup>+0.24</sup> <sub>-0.16</sub>	1.26 <sup>+0.30</sup> <sub>-0.17</sub>	9.13 <sup>+1.45</sup> <sub>-1.33</sub>	8.81 <sup>+2.32</sup> <sub>-1.83</sub>	11.97 <sup>+1.34</sup> <sub>-1.79</sub>	8.83 <sup>+1.84</sup> <sub>-1.51</sub>	0.30 <sup>+0.24</sup> <sub>-0.19</sub>	0.82 <sup>+0.09</sup> <sub>-0.15</sub>	47.54 <sup>+31.02</sup> <sub>-25.32</sub>	46.18 <sup>+30.56</sup> <sub>-24.40</sub>
17	1.30 <sup>+0.30</sup> <sub>-0.20</sub>	1.35 <sup>+0.35</sup> <sub>-0.22</sub>	11.10 <sup>+2.00</sup> <sub>-1.74</sub>	8.72 <sup>+3.31</sup> <sub>-2.46</sub>	11.47 <sup>+1.59</sup> <sub>-1.91</sub>	8.69 <sup>+2.17</sup> <sub>-1.78</sub>	0.32 <sup>+0.22</sup> <sub>-0.20</sub>	0.75 <sup>+0.17</sup> <sub>-0.36</sub>	49.82 <sup>+30.33</sup> <sub>-26.46</sub>	40.93 <sup>+31.02</sup> <sub>-21.21</sub>
18	1.41 <sup>+0.34</sup> <sub>-0.25</sub>	1.47 <sup>+0.41</sup> <sub>-0.29</sub>	10.49 <sup>+1.86</sup> <sub>-1.77</sub>	12.61 <sup>+2.15</sup> <sub>-2.49</sub>	11.37 <sup>+1.66</sup> <sub>-1.91</sub>	10.03 <sup>+1.50</sup> <sub>-1.59</sub>	0.26 <sup>+0.21</sup> <sub>-0.17</sub>	0.81 <sup>+0.07</sup> <sub>-0.10</sub>	38.42 <sup>+31.47</sup> <sub>-19.84</sub>	37.51 <sup>+31.02</sup> <sub>-19.39</sub>
19	1.58 <sup>+0.47</sup> <sub>-0.35</sub>	1.71 <sup>+0.40</sup> <sub>-0.37</sub>	9.21 <sup>+2.15</sup> <sub>-1.80</sub>	9.01 <sup>+1.89</sup> <sub>-2.03</sub>	12.03 <sup>+1.33</sup> <sub>-2.00</sub>	11.10 <sup>+1.84</sup> <sub>-2.25</sub>	0.33 <sup>+0.25</sup> <sub>-0.21</sub>	0.74 <sup>+0.13</sup> <sub>-0.22</sub>	46.86 <sup>+30.79</sup> <sub>-24.86</sub>	44.81 <sup>+30.79</sup> <sub>-23.49</sub>
20	1.63 <sup>+0.42</sup> <sub>-0.36</sub>	1.56 <sup>+0.41</sup> <sub>-0.33</sub>	11.16 <sup>+1.97</sup> <sub>-1.86</sub>	10.11 <sup>+2.52</sup> <sub>-2.29</sub>	12.09 <sup>+1.27</sup> <sub>-1.84</sub>	9.70 <sup>+1.96</sup> <sub>-1.86</sub>	0.27 <sup>+0.22</sup> <sub>-0.17</sub>	0.83 <sup>+0.08</sup> <sub>-0.13</sub>	49.82 <sup>+30.33</sup> <sub>-26.68</sub>	44.12 <sup>+29.88</sup> <sub>-22.81</sub>
21	1.42 <sup>+0.37</sup> <sub>-0.26</sub>	1.78 <sup>+0.40</sup> <sub>-0.41</sub>	10.64 <sup>+1.71</sup> <sub>-1.54</sub>	12.26 <sup>+1.86</sup> <sub>-2.44</sub>	12.26 <sup>+1.17</sup> <sub>-1.71</sub>	11.83 <sup>+1.37</sup> <sub>-1.98</sub>	0.26 <sup>+0.21</sup> <sub>-0.16</sub>	0.82 <sup>+0.08</sup> <sub>-0.13</sub>	41.84 <sup>+31.47</sup> <sub>-22.12</sub>	38.42 <sup>+30.56</sup> <sub>-19.84</sub>
22	1.33 <sup>+0.28</sup> <sub>-0.21</sub>	1.47 <sup>+0.42</sup> <sub>-0.30</sub>	10.11 <sup>+1.51</sup> <sub>-1.48</sub>	9.74 <sup>+2.84</sup> <sub>-2.29</sub>	11.83 <sup>+1.40</sup> <sub>-1.79</sub>	7.91 <sup>+1.87</sup> <sub>-1.60</sub>	0.26 <sup>+0.21</sup> <sub>-0.17</sub>	0.83 <sup>+0.09</sup> <sub>-0.16</sub>	43.21 <sup>+31.93</sup> <sub>-22.81</sub>	47.32 <sup>+30.56</sup> <sub>-25.09</sub>
23	2.01 <sup>+0.42</sup> <sub>-0.42</sub>	-	11.85 <sup>+1.68</sup> <sub>-1.74</sub>	-	12.36 <sup>+1.10</sup> <sub>-1.67</sub>	-	0.33 <sup>+0.24</sup> <sub>-0.21</sub>	-	46.86 <sup>+30.33</sup> <sub>-24.86</sub>	-
24	1.40 <sup>+0.33</sup> <sub>-0.24</sub>	1.76 <sup>+0.40</sup> <sub>-0.40</sub>	10.52 <sup>+1.65</sup> <sub>-1.51</sub>	12.14 <sup>+1.97</sup> <sub>-2.64</sub>	12.32 <sup>+1.14</sup> <sub>-1.67</sub>	11.65 <sup>+1.49</sup> <sub>-2.14</sub>	0.27 <sup>+0.22</sup> <sub>-0.17</sub>	0.80 <sup>+0.09</sup> <sub>-0.15</sub>	45.95 <sup>+31.93</sup> <sub>-24.63</sub>	50.74 <sup>+30.56</sup> <sub>-27.14</sub>
25	1.42 <sup>+0.35</sup> <sub>-0.26</sub>	1.40 <sup>+0.33</sup> <sub>-0.25</sub>	9.79 <sup>+1.74</sup> <sub>-1.59</sub>	9.27 <sup>+1.68</sup> <sub>-2.00</sub>	12.34 <sup>+1.13</sup> <sub>-1.73</sub>	11.90 <sup>+1.42</sup> <sub>-2.05</sub>	0.27 <sup>+0.23</sup> <sub>-0.17</sub>	0.72 <sup>+0.12</sup> <sub>-0.19</sub>	50.51 <sup>+30.33</sup> <sub>-27.14</sub>	49.82 <sup>+30.56</sup> <sub>-26.68</sub>
26	1.48 <sup>+0.50</sup> <sub>-0.31</sub>	1.88 <sup>+0.43</sup> <sub>-0.42</sub>	10.17 <sup>+1.83</sup> <sub>-1.83</sub>	13.59 <sup>+1.51</sup> <sub>-2.29</sub>	11.88 <sup>+1.42</sup> <sub>-2.13</sub>	12.04 <sup>+1.18</sup> <sub>-1.65</sub>	0.35 <sup>+0.27</sup> <sub>-0.22</sub>	0.76 <sup>+0.09</sup> <sub>-0.13</sub>	37.51 <sup>+30.56</sup> <sub>-19.16</sub>	37.05 <sup>+30.56</sup> <sub>-18.93</sub>
27	1.38 <sup>+0.30</sup> <sub>-0.24</sub>	1.42 <sup>+0.37</sup> <sub>-0.25</sub>	8.46 <sup>+1.51</sup> <sub>-1.30</sub>	7.18 <sup>+2.20</sup> <sub>-1.39</sub>	12.02 <sup>+1.30</sup> <sub>-1.84</sub>	8.27 <sup>+2.09</sup> <sub>-1.45</sub>	0.34 <sup>+0.25</sup> <sub>-0.22</sub>	0.76 <sup>+0.13</sup> <sub>-0.25</sub>	42.07 <sup>+31.47</sup> <sub>-22.12</sub>	35.68 <sup>+28.96</sup> <sub>-17.79</sub>
Combined burst	1.36 <sup>+0.07</sup> <sub>-0.07</sub>	1.21 <sup>+0.05</sup> <sub>-0.05</sub>	9.9 <sup>+0.4</sup> <sub>-0.4</sub>	7.0 <sup>+0.4</sup> <sub>-0.4</sub>	12.2 <sup>+0.4</sup> <sub>-0.5</sub>	7.2 <sup>+0.3</sup> <sub>-0.4</sub>	0.16 <sup>+0.05</sup> <sub>-0.04</sub>	0.84 <sup>+0.01</sup> <sub>-0.01</sub>	26.9 <sup>+5.3</sup> <sub>-4.4</sub>	27.8 <sup>+6.7</sup> <sub>-4.3</sub>

**Table 3.** Medians and 68% credible intervals of the mass, radius, distance, observer's inclination, and column density for each burst and when information from all of the bursts is combined, for the Bkg free and Bkg constrained (con) cases.

Although the absence of an X-ray eclipse during the XTE J1814–338 outburst implies that  $\cos(i) > 0.2$  (Krauss et al. 2005), we refrained from enforcing this constraint in our prior on the observer inclination. Instead, we opted for a significantly broader prior distribution. In the Bkg free scenario, only half of the posterior samples are consistent with the absence of an eclipse.

Given these issues, it is clear that when the background is unconstrained, the preferred solution likely does not reflect correctly the properties of XTE J1814–338. In what follows we therefore discuss only the Bkg constrained case.

#### 4.1.2 Bkg constrained case

When we constrain the background, we find a mass of  $1.21^{+0.05}_{-0.05} M_{\odot}$ , a radius of  $7.0^{+0.4}_{-0.4}$  km, with the NS located at a distance of  $7.2^{+0.3}_{-0.4}$  kpc. The inferred radius is small compared to values inferred from other astrophysical and laboratory measurements (see e.g. Raaijmakers et al. 2021; Huth et al. 2022). While the median

radius, marginalized over other parameters, for individual bursts, is typically greater than 8 km, a contrasting trend emerges when combining the information from all bursts. This discrepancy arises from the fact that the joint posterior distribution of mass, radius, and distance have a wide scatter for each burst, with regions of high probabilities around 10 km. Yet, the slopes of correlations among mass, radius, and distance are different, and the posteriors of different bursts intercept in regions of lower radii. Consequently, when combining results from all bursts, only regions within the radius space featuring smaller values exhibit high posteriors, thereby yielding the small inferred radius. The small inferred radius when all bursts are combined, coupled with the fact that the rms FA of the bolometric pulse of each burst especially for the first harmonic reaches lower values than that of the data, suggests that a single hot spot model might not be adequate to explain the burst oscillation properties.

In the Bkg constrained scenario, the background contribution to the burst is relatively low compared to the contribution from



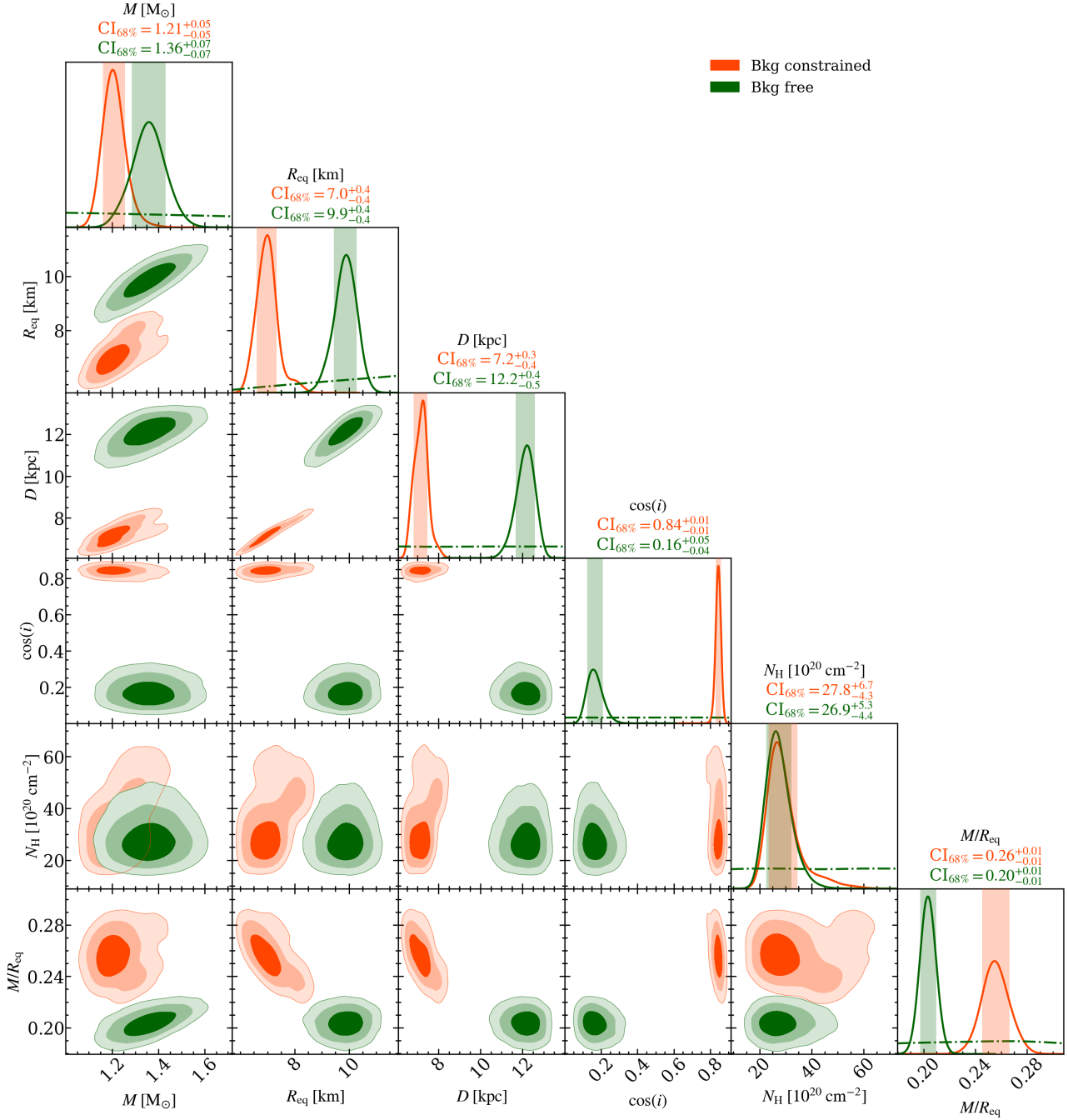


**Figure 4.** Combined posterior distributions of mass, radius, distance, observer inclination, column density, and compactness. The two-dimensional posterior distributions are, from most opaque to least, the 68%, 95%, and 99% posterior credible region. The solid (dash-dotted) lines along the diagonal represent the marginalized posterior (prior) distribution of each parameter. The vertical bands are the inferred 68% credible intervals.

the hot spot. The bursts are predominantly dominated by photons emitted from the hot spot, while the stellar counts remain relatively low. This depiction aligns more closely with our current understanding of Type I X-ray burst physics. However, there are still five bursts where the number of counts from the background is either higher or nearly equal to the number of counts from the hot spot. This is due to how we define the start of the burst which led to a high pre-burst count rate for these bursts. Our simplistic assumption, that the upper limit on the background is the upper value of  $f_a$  scaling factor times the pre-burst spectrum led to a big upper limit on the

background, especially for faint bursts. Therefore, obtaining a better understanding of the background behavior during a burst is essential for future analyses.

Constraining the background leads to a consistent distance estimate obtained using Concord (see Figure 8) assuming a hydrogen-rich burst. However, this distance estimate cannot be compared directly to those reported by [Baglio et al. \(2013\)](#) and [Strohmayer et al. \(2003\)](#) since a  $1.4 M_{\odot}$  was assumed in these works and we are now inferring a lower value. Employing the methodology of

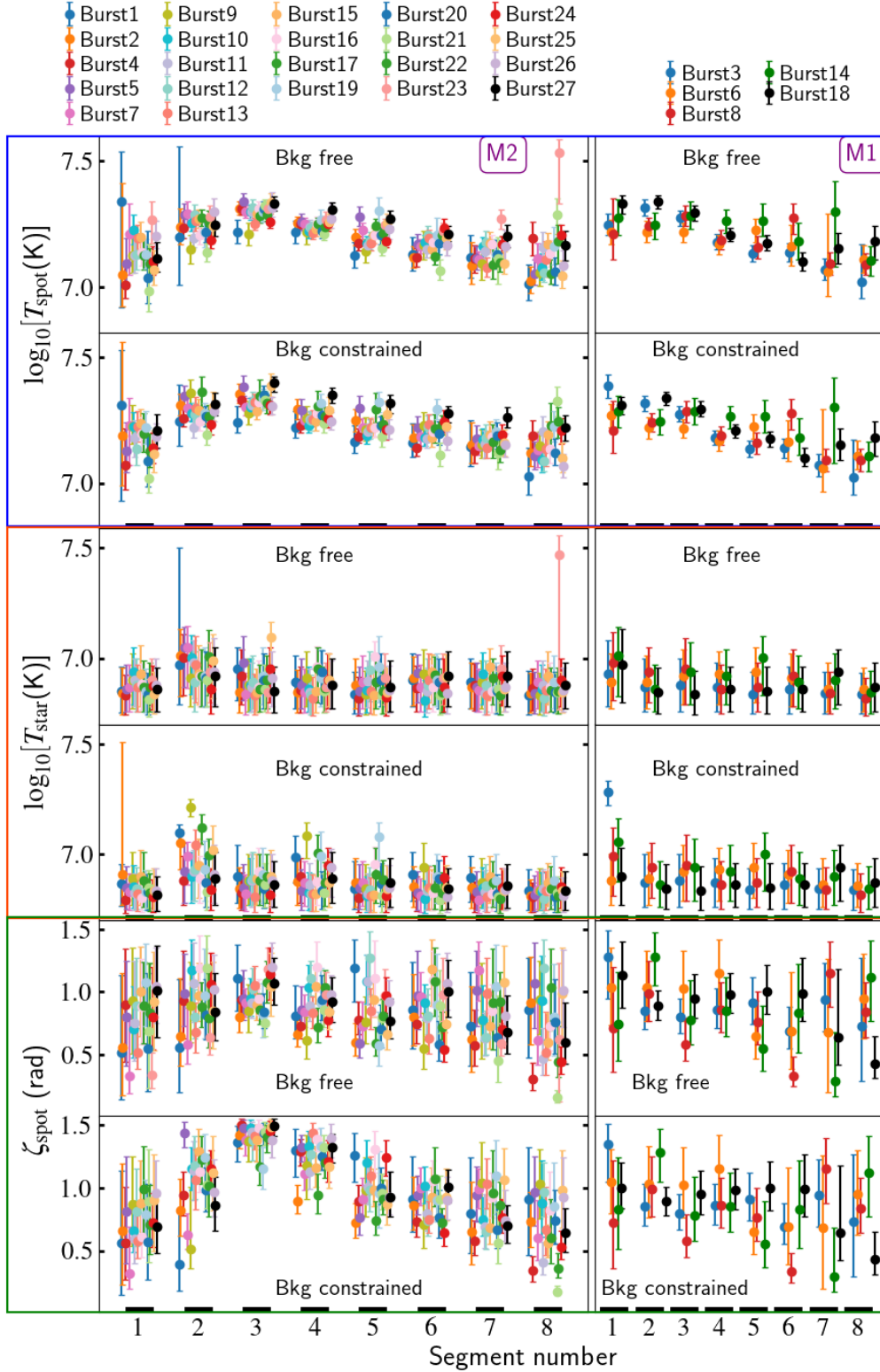


**Figure 5.** Time evolution of the hot spot temperature, star temperature, and angular radius of the hot spot. The left panel shows these parameters' evolution for bursts categorized as M2, while the right panel depicts bursts categorized as M1.

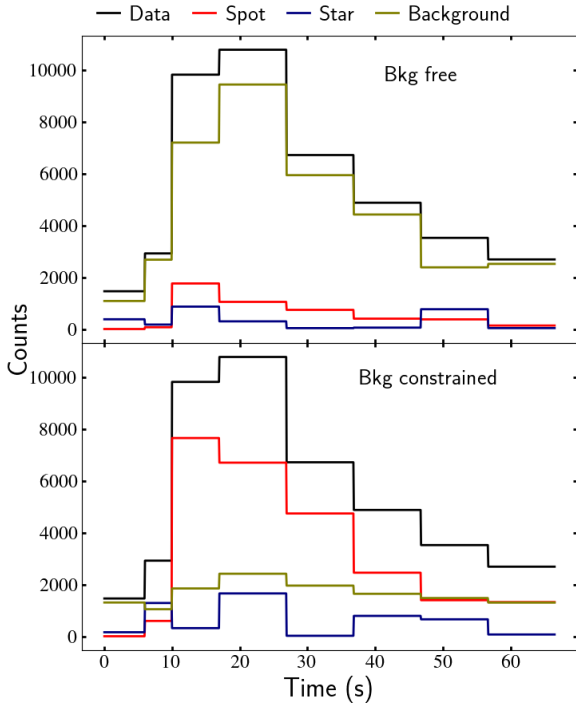


**Figure 6.** Temporal evolution in counts for Burst 1, showing contributions from the hot spot, the rest of the star, and the background. The counts are obtained using the maximum likelihood solution. In the *Bkg free* case, most of the burst photons originate from the background rather than any emitting component (hot spot & star) on the stellar surface. However, once background constraints are applied (*Bkg constrained*), this situation changes and aligns more closely with the physical understanding of how bursts occur.

Strohmayer et al. (2003), we derive a distance of  $7.7^{+1.5}_{-1.5}$  assuming a  $1.21 M_{\odot}$  NS, which aligns well with our inferred distance.

All samples for the observer’s inclination agree with the absence of an eclipse (Krauss et al. 2005). Furthermore, our findings are consistent (across the entire posterior distribution) with those of Krauss et al. (2005), where it was inferred from the magnitude limit of the optical counterpart that  $\cos(i) \lesssim 0.93$ .

Regarding the line-of-sight hydrogen column density, our results are higher than the commonly reported range of  $(16 - 17) \times 10^{20} \text{ cm}^{-2}$ , a prevalent finding within the existing literature concerning XTE J1814–338 (see e.g., Krauss et al. 2005; Galloway et al. 2020). These line-of-sight hydrogen column densities are computed using Dickey & Lockman (1990) HI column density<sup>5</sup>. The line-of-sight hydrogen column density is also higher than  $15^{+2.1}_{-1.9} \times 10^{20} \text{ cm}^{-2}$  obtained using the 3D interstellar absorption map (Doroshenko 2024)<sup>6</sup>.

## 4.2 Implications for Equation of State

In the *Bkg constrained* case, where the physics aligns with our current understanding of Type I X-ray bursts mechanism, we found

<sup>5</sup> <https://cxc.harvard.edu/toolkit/colden.jsp>

<sup>6</sup> <http://astro.uni-tuebingen.de/nh3d/nhtool>

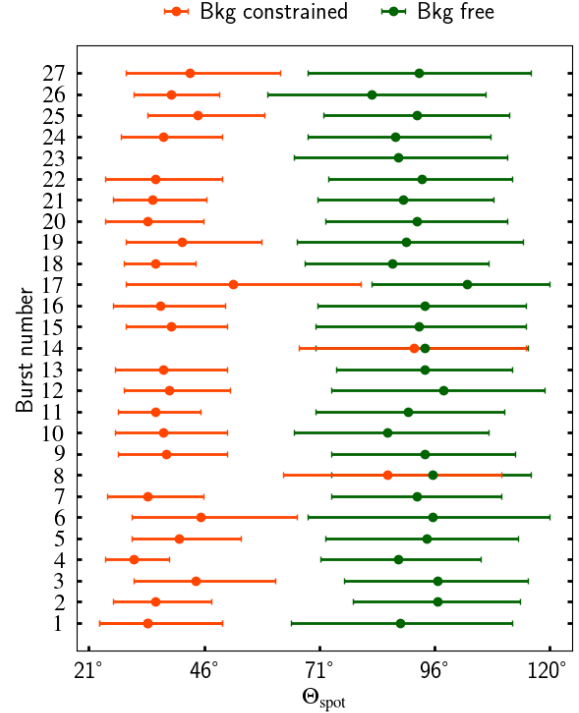


**Figure 7.** Median and the 68% credible interval of the co-latitude of the centre of the hot spot for each burst. In the *Bkg constrained* case, the results are not shown for Burst 23 given that the run had to be halted due to high computational cost (see Section 3).

a  $1.21^{+0.05}_{-0.05} M_{\odot}$  star with a radius of  $7.0^{+0.4}_{-0.4}$  km, indicating a preference for softer EoSs. The NICER collaboration has inferred the mass and radius of two NS. One has a high mass (about  $2.0 M_{\odot}$ ), with tight mass constraints inferred from radio observations (Cromartie et al. 2020), PSR J0740+6620 (Miller et al. 2021; Riley et al. 2021; Salmi et al. 2022). The second, PSR J0030+0451 had no mass prior constraint. Initial analyses suggested a mass of about  $1.4 M_{\odot}$  and a radius of about 13 km (Miller et al. 2019; Riley et al. 2019). Updated analysis, using a new NICER response and improved background constraints from XMM-Newton (Vinciguerra et al. 2024), found a mode compatible with a canonical neutron star with a lower radius of  $11.71^{+0.88}_{-0.83}$  km (68% CI).

By fitting the X-ray burst cooling tail spectra of 4U 1702–429 with different models, Nättilä et al. 2017 derived for one of the models considered -model  $\mathcal{A}$ -that 4U 1702–429 could be a canonical star with a radius of  $R_{1.4} = 12.4^{+0.4}_{-0.4}$  km (68% CI). Although model  $\mathcal{A}$  was not the preferred model, it would be broadly consistent with the NICER results for the radius of a  $1.4 M_{\odot}$  star.

The radius of a  $1.4 M_{\odot}$  star has also been derived through EoS inference. By integrating multiple pieces of information, including tidal deformability data from the gravitational wave event GW170817 (Abbott et al. 2017) and measurements from both PSR J0030+0451 and PSR J0740+6620, and applying EoS inference techniques, both Miller et al. 2021 and Raaijmakers et al. 2021 arrived at similar results, indicating a radius of approximately  $R_{1.4} \approx 12$  km. Radii measurements from tidal deformability from the gravitational wave event GW170817 also favor softer EoS (Abbott et al. 2018). Similar results have been obtained by other groups,

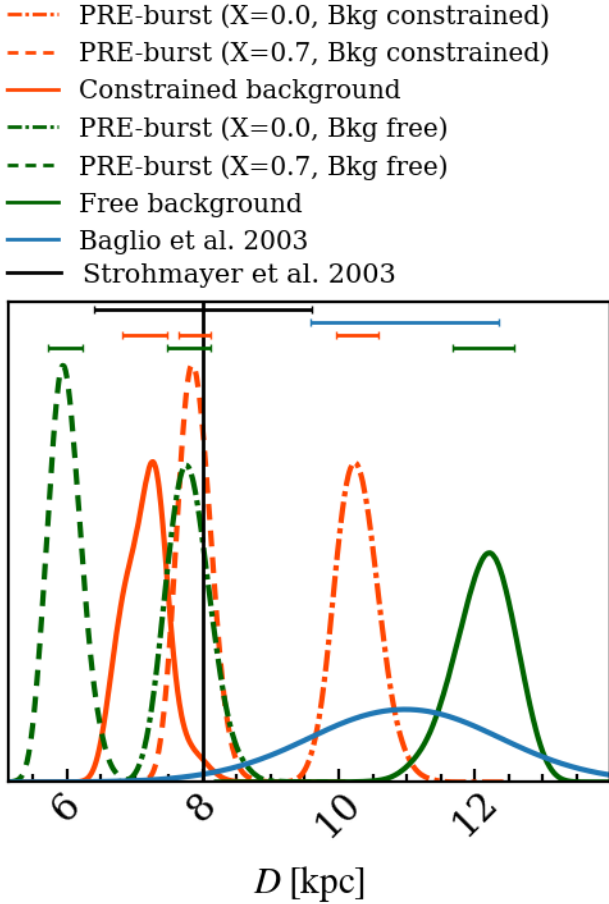


**Figure 8.** Posterior distributions of the distance. The color-coded horizontal segments are the 68% credible intervals of each distribution symmetric in marginal posterior mass about the median. In the *Strohmayer et al. (2003)* case, the horizontal segment is the 20% uncertainty on the inferred distance. PRE-burst (X, "B") denotes that the distance distribution is computed using Concord, assuming a hydrogen fraction of X, along with the median of the mass and radius, and observer inclination distribution obtained under the "B" assumption, where "B" is either Bkg free or Bkg constrained.

see for example *Huth et al. (2022)*, whose EoS analysis yields  $R_{1.4} = 12.01^{+0.78}_{-0.77}$  km.

All the above-mentioned results are broadly consistent with each other. However, the radius inferred for XTE J1814–338 is notably smaller than the radius expected for a  $1.2 M_{\odot}$  NS (see e.g. *Raaijmakers et al. 2021; Huth et al. 2022*), which may imply limitations in our single hot spot model's ability to depict the data accurately. However, the possibility of such a small radius cannot be ruled out, especially when considering the presence of strong phase transitions in quantum chromodynamics. Such a phase transition would allow hybrid stars, in the second branch, with considerably smaller radii than the current constraints (*Christian & Schaffner-Bielich 2022; Jie Li et al. 2024*).

#### 4.3 Burst and burst oscillation properties: Bkg constrained case

The evolution of the star's temperature, the hot spot temperature, and the hot spot angular radius for each burst suggest that the burning

that occurred on XTE J1814–338 during its 2003 outburst was confined. This is mainly because photons originating from the hot spot dominate the burst emission, coupled with the fact that the hot spot temperature and the hot spot angular radius change over time while the stellar temperature remains constant. Remarkably the stellar temperature remains relatively low, about  $(0.64 \pm 0.16)$  keV throughout all bursts. The temperature is consistent with the X-ray spectral properties inferred by *Krauss et al. (2005)* for XTE J1814–338 during its outburst.

If the spot locations reflect the starting point of the bursts, then ignition mostly occurs halfway between XTE J1814–338's equator and its northern rotational pole. The flames then propagate and engulf about half of the star before dying out. Given the weak magnetic field expected for XTE J1814–338 fast rotation is likely what halts the flames from spreading across the entire surface (*Cavecchi et al. 2016*). However, the ignition location is challenging to reconcile with the hypothesis that ignition is more likely to take place at the equator, mainly due to the influence of rapid rotation, which reduces effective gravity in that area (*Spitkovsky et al. 2002; Cooper & Narayan 2007*). The possibility of channeled accretion leading to off-equatorial ignition in pulsars has been explored, but as yet no mechanism has been identified (*Goodwin et al. 2021*).

It is important to note that there are significant uncertainties associated with the inferred time-varying parameters. For example, the 99% credible regions for the majority of the angular radii of each segment are nearly identical to the prior space. In *Kini et al. (2024b)*, the uncertainties associated with time-varying parameters were considerably lower. This was primarily due to the hierarchical evolution imposed on the time-varying parameters coupled with tight constraints on both the distance and the background. In addition to the lack of constraints on time-varying parameters in this work, the significant level of uncertainty can be attributed to several factors. Firstly, the quality of the available data might not be sufficient to fully capture the complex behavior of the hot spot during the burst. Secondly, the duration of each time segment could be too lengthy to detect subtle variations. As a result, drawing definitive conclusions about the evolution of temporally varying parameters within each burst becomes challenging based solely on this analysis. Given these limitations, it becomes apparent that obtaining improved data quality is desirable. Moreover, the necessity for more computing resources becomes evident for understanding the parameter evolutions during the burst.

#### 4.4 Comparison with previous analyses of XTE J1814–338

*Bhattacharyya et al. (2005)* have modeled the TBOs of 22 bursts of XTE J1814–338 using a single hot spot model as in this paper. However, there are some major differences in the analysis approach e.g.: *Bhattacharyya et al. 2005* did not incorporate time variability in their analysis, nor did they consider the effects of the interstellar medium, and the temperature of the hot spot was fixed at 2 keV. Moreover, bursts were stacked during the modelling procedure, they considered a spherical star with frame dragging, and the entire analysis was conducted assuming two EoS. Their analysis yielded constraints on the compactness, suggesting  $M/R_{\text{eq}} < 1/4.2 \approx 0.238$  at a 90% confidence level<sup>7</sup>. They also determined the center of the hot spot ( $\Theta_{\text{spot}}$ ) to be within the range of  $60^\circ$  to  $139^\circ$  (with regions of  $\Theta_{\text{spot}} < 50^\circ$  being deemed highly unlikely), at a 90% confidence level. Moreover, they identified a high probability for  $i > 22^\circ$ . Our results also

<sup>7</sup> As in Figure 4, we set  $G=c=1$ .



align with their lower limit on the observer inclination but only approximately 5% of the inferred posterior mass of compactness is below their compactness upper limit for the Bkg constrained case. Also, we observed a discrepancy regarding the center of the hot spot; our findings suggest that for most bursts, the most probable location lies between  $20^\circ$  and  $50^\circ$ , whereas [Bhattacharyya et al. 2005](#) identified this range as highly unlikely. Another study that has constrained the properties of XTE J1814–338 is that conducted by [Wang et al. \(2017\)](#). Through phase-resolved spectroscopy of its 2003 outburst, they derived a mass of  $2.0^{+0.7}_{-0.5} M_\odot$  with their lower limit being higher than our 68% CI upper limit. Assuming a pulsar mass of  $1.4 M_\odot$ , they concluded that  $i \gtrsim 48^\circ$ . Such constraint on the observer inclination does not align with the inferred posterior for the inclination in the Bkg constrained case, where all our samples have  $i < 48^\circ$ . It is crucial to highlight that their assumption of the mass does not align with the mass inferred under Bkg constrained case. Also, the prior space for  $i^8$  assumed in their analysis inherently excludes our most probable solutions.

Using the accretion-powered pulsations (not the TBOs), [Leahy et al. \(2009\)](#) have also inferred properties of XTE J1814–338. By fitting the bolometric pulse profiles of two bands (2–3 keV, and 7–9 keV) and using a single hot spot model and 23 days of observation from June 5–27, 2003, and excluding the X-bursts, the analysis mostly yielded high inferred mass and stiff equations of state solutions. Our analysis however favours a soft EoS solution.

#### 4.5 Improvements to this analysis

There are a couple of aspects that our analysis has not thoroughly explored, some due to limited computing resources, and some for the lack of knowledge of the underlying physics. It would be beneficial to delve into these aspects in future research.

First, we assume that the atmosphere of XTE J1814–338 is that of a thermonuclear burster. However it is possible that such an atmosphere model might not correctly describe the physical conditions of XTE J1814–338, if the pulsations originate from somewhere in the atmosphere. Second, we presumed that the atmosphere composition of XTE J1814–338 has solar abundance. This is mainly because the burst morphology strongly suggests a burning of hydrogen and helium ([Galloway et al. 2008](#)). However, we cannot rule out the possibility that the atmospheric composition could be different<sup>9</sup>. It is also possible that the fraction of heavier elements in the atmosphere composition is different from what we currently assume ( $Z = 0.0134$ ). Investigating how variations in atmospheric composition might influence the inferred parameters, particularly the mass and radius is therefore desirable. Yet, we note that given the data quality of the bursts, the sensitivity of our results to changes in atmosphere composition through pulse profile modelling might be limited.

We also employed a single uniform temperature hot spot to model the observed oscillations in the burst light curves. No discernible anomalies within the residuals or in the residual distributions indicate inadequate model performance. Nevertheless, the challenge of fitting the harmonic contents of the data with a single hot spot, along with the small inferred radius, hints at potential

systematic bias. We could explore the impact of an additional constraint, ensuring that both the rms FA of the bolometric pulse, for both the fundamental and the first harmonic, match that of the data during sampling. Also given that XTE J1814–338 is an AMXP, it exhibits pulsations arising from the accretion hot spot(s) as well. It is highly plausible that the hot spot causing burst oscillations is distinct from those generating accretion pulsations (see e.g. [Watts et al. 2008](#); [Cavecchi & Patruno 2022](#)). Therefore, the observed pulsations could potentially be a combined result of these hot spots: a burst oscillation hot spot and one or two (depending on whether the star is assumed to be entirely visible or not) hot spots due to the accretion. While during the peak of the burst, the contribution from accretion pulsations is supposed to be negligible due to the dominance of burst oscillations ([Watts et al. 2005](#)), this might not hold true at the burst’s start and end. Notably, the accretion hot spot’s temperature is estimated to be  $\sim 1$  keV ([Poutanen & Gierliński 2003](#); [Salmi et al. 2018](#); [Das et al. 2022](#)), which coincidentally aligns with the temperature we determined for the burst oscillation at the tail and beginning of the bursts. This is a possible explanation for the increase in the hot spot temperature observed in the tail of the bursts. Ideally, exploring scenarios involving multiple hot spots would be insightful and potentially yield much higher rms FA of the first harmonic.

Furthermore, given that XTE J1814–338 is an AMXP, it is surrounded by both an accretion column and an accretion disk. It is possible that the influence of both these components could impact the observed spectrum but in this work, we overlooked both of them. The effects of the accretion disk should, in theory, be less pronounced, as they would predominantly affect the lower energy photons where RXTE is less sensitive. Nevertheless, it is desirable to scrutinize the effects of this component in more detail. Furthermore, we assumed that the entire star remains visible throughout the burst given that the burst might push away the accretion disk (see e.g. [Fragile et al. 2020](#)), rendering both hemispheres of the star visible. But such a scenario is plausible during PRE bursts, which the bursts analyzed in this analysis are not. Moreover, possibly obscuration from accretion was overlooked.

Finally, we kept the phase and co-latitude of the hot spot fixed across all time segments. Nevertheless, previous analysis of XTE J1814–338 has shown a phase drift of up to 10% for some bursts ([Cavecchi & Patruno 2022](#)). Although we checked that this phase drift does not significantly impede parameter inference for synthetic data with  $10^5$  counts, ignoring this phase drift might pose issues when combining bursts. Ideally, we should leave both the phase of the hot spot and the co-latitude of the hot spot free for each segment. However, this would lead to extra computational time.

## 5 CONCLUSION

We have conducted a comprehensive analysis of the AMXP and TBO source XTE J1814–338 to infer its properties through the PPM of burst oscillations observed during its 2003 outburst. To achieve this, we employed a state-of-the-art PPM technique to derive key parameters such as the mass, radius, distance, and observer’s inclination of XTE J1814–338.

Our analysis yielded the following results for XTE J1814–338: a mass of  $1.21^{+0.05}_{-0.05} M_\odot$ , a radius of  $7.0^{+0.4}_{-0.4}$  km, and a distance of  $7.2^{+0.3}_{-0.4}$  kpc. Our result favors soft EoS for NSs. However, the relatively small radius inferred and the lack of harmonic content in the bolometric pulse may stem from potential systematic errors originating from our limited understanding of burst oscillation mecha-

<sup>8</sup> For the prior on the observer inclination, they have  $\cos(i) \sim \mathcal{U}(\cos(35^\circ), \cos(78^\circ))$ .

<sup>9</sup> For XTE J1814–338, pure helium burning is highly improbable, since if it were to occur, the resulting burst shapes are expected to differ significantly from those observed in the 2003 bursts.

nisms. Therefore, further research to enhance our understanding of burst oscillation origins would be invaluable. Furthermore, while a previous analysis (Bhattacharyya et al. 2005) used a single uniform temperature hot spot model for burst oscillations, our analysis indicates potential shortcomings in this model once time variability is fully taken into account, highlighting the necessity for alternative models.

Moreover, potential systematic biases originating from other various modelling assumptions made in this paper cannot be ruled out. Given that XTE J1814–338 is an AMXP, modelling the accretion pulsations through PPM, investigating burst properties as for IGR J17498–2921 (Galloway et al. 2024) or SAX J1808.4–3658 (Goodwin et al. 2021; Galloway et al. 2024) or applying the direct cooling tail method (see e.g. Nättilä et al. 2017; Molkov et al. 2024) would be valuable. By doing so, we can cross-check results and mitigate potential biases associated with PPM of TBO sources. Additionally, the correlation between the mass, radius, and distance varies for each burst, leading to the small inferred radius when combining the information from many bursts. Independent constraints on the distance would significantly improve future analyses of this source.

With about 2 million total counts, the uncertainties on both the mass and radius are about 10% (using the 68% CI). If XTE J1814–338-like bursts would be observed with proposed large-area X-ray spectral-timing telescopes like the enhanced X-ray Timing and Polarimetry mission (e-XTP) (e.g., Zhang et al. 2019; Watts et al. 2019), or the Spectroscopic Time-Resolving Observatory for Broadband Energy X-rays (STROBE-X) (e.g., Ray et al. 2019), this would result in much larger number of counts collected, hence reducing the uncertainties to only a few percent. This underscores the significance of modelling burst oscillation sources.

Our analysis also delved into the temporal evolution of hot spot temperatures, angular radii, and stellar temperatures during the bursts. While we observed marginal variation during the bursts of the hot spot temperature and the hot spot angular radius, the stellar temperature remained stable. This suggests a preference for confined burning where the flames initially spread across half the stellar surface and then stall.

However, it is important to note that the quality of the available data, the number of each time segment used, and the absence of independent constraints on certain parameters, such as distance and background, have made it challenging to draw definitive conclusions regarding the true evolution of the time-dependent parameters. To gain deeper insights into the poorly understood physics underlying the burst and burst oscillations, improved data quality, increased computational resources, independent distance measurements and better knowledge of the atmosphere composition are highly desirable.

Additionally, although trying different background constraints yielded similar results in terms of mass, the inferred radius, distance, and observer inclination exhibited significant disparities. This underscores the importance of independent constraints on both distance and observer inclination to gain a better understanding of the poorly constrained background behavior during a Type I X-ray burst.

In sum, this study has provided insights into probable properties of XTE J1814–338 and underscores the challenges and opportunities inherent in inferring TBOs sources properties through PPM. Future observations and modelling efforts will undoubtedly continue to enhance our understanding of NSs and the fundamental physics governing their behavior.

## ACKNOWLEDGEMENTS

YK, TS, SV, and ALW acknowledge support from ERC Consolidator Grant No. 865768 AEONS (PI Watts). This work was carried out on the HELIOS cluster, mostly on dedicated nodes funded via the abovementioned ERC CoG. EvdW contributed to this work as part of her Masters thesis project, and GPK as part of his Bachelor Project, both at UvA. SB acknowledges support from NASA grant 80NSSC22K0728. VS acknowledges support by Deutsche Forschungsgemeinschaft (DFG; grant WE 1312/59-1).

## DATA AVAILABILITY

All the data, posterior samples as well as the scripts used for the runs and plots are available on Zenodo (Kini et al. 2024a).

## REFERENCES

- Abbott B. P., et al., 2017, *Phys. Rev. Lett.*, **119**, 161101  
 Abbott B. P., et al., 2018, *Phys. Rev. Lett.*, **121**, 161101  
 Alizai K., et al., 2023, *MNRAS*, **521**, 3608  
 Baglio M. C., D’Avanzo P., Muñoz-Darias T., Breton R. P., Campana S., 2013, *A&A*, **559**, A42  
 Bauböck M., Psaltis D., Özel F., Johannsen T., 2012, *ApJ*, **753**, 175  
 Baym G., Hatsuda T., Kojo T., Powell P. D., Song Y., Takatsuka T., 2018, *Rept. Prog. Phys.*, **81**, 056902  
 Beloborodov A. M., 2002, *ApJ*, **566**, L85  
 Bhattacharyya S., Strohmayer T. E., Miller M. C., Markwardt C. B., 2005, *ApJ*, **619**, 483  
 Bildsten L., 1998, in Buccheri R., van Paradijs J., Alpar A., eds, *NATO Advanced Study Institute (ASI) Series C Vol. 515, The Many Faces of Neutron Stars*. p. 419 ([arXiv:astro-ph/9709094](https://arxiv.org/abs/astro-ph/9709094))  
 Bogdanov S., et al., 2019, *ApJ*, **887**, L26  
 Bogdanov S., et al., 2021, *ApJ*, **914**, L15  
 Braje T. M., Romani R. W., Rauch K. P., 2000, *ApJ*, **531**, 447  
 Buchner J., et al., 2014, *A&A*, **564**, A125  
 Cadeau C., Morsink S. M., Leahy D., Campbell S. S., 2007, *ApJ*, **654**, 458  
 Cavecchi Y., Patruno A., 2022, *MNRAS*, **510**, 1431  
 Cavecchi Y., Watts A. L., Braithwaite J., Levin Y., 2013, *MNRAS*, **434**, 3526  
 Cavecchi Y., Watts A. L., Levin Y., Braithwaite J., 2015, *MNRAS*, **448**, 445  
 Cavecchi Y., Levin Y., Watts A. L., Braithwaite J., 2016, *MNRAS*, **459**, 1259  
 Chambers F. R. N., Watts A. L., 2020, *MNRAS*, **491**, 6032  
 Chambers F. R. N., Watts A. L., Keek L., Cavecchi Y., Garcia F., 2019, *ApJ*, **871**, 61  
 Chen K., Shaham J., 1989, *ApJ*, **339**, 279  
 Christian J.-E., Schaffner-Bielich J., 2022, *ApJ*, **935**, 122  
 Cooper R. L., Narayan R., 2007, *ApJ*, **657**, L29  
 Cromartie H. T., et al., 2020, *Nature Astronomy*, **4**, 72  
 Das P., Porth O., Watts A. L., 2022, *MNRAS*, **515**, 3144  
 Dickey J. M., Lockman F. J., 1990, *ARA&A*, **28**, 215  
 Doroshenko V., 2024, *arXiv e-prints*, p. [arXiv:2403.03127](https://arxiv.org/abs/2403.03127)  
 Feroz F., Hobson M. P., 2008, *MNRAS*, **384**, 449  
 Feroz F., Hobson M. P., Bridges M., 2009, *MNRAS*, **398**, 1601  
 Feroz F., Hobson M. P., Cameron E., Pettitt A. N., 2019, *The Open Journal of Astrophysics*, **2**, 10  
 Fragile P. C., Ballantyne D. R., Blankenship A., 2020, *arXiv e-prints*, p. [arXiv:2001.01032](https://arxiv.org/abs/2001.01032)  
 Gaia Collaboration et al., 2016, *A&A*, **595**, A1  
 Galloway D. K., Muno M. P., Hartman J. M., Psaltis D., Chakrabarty D., 2008, *ApJS*, **179**, 360  
 Galloway D. K., et al., 2020, *ApJS*, **249**, 32  
 Galloway D. K., Johnston Z., Goodwin A., He C.-C., 2022, *ApJS*, **263**, 30

- Galloway D. K., Goodwin A. J., Hilder T., Waterson L., Cupák M., 2024, [arXiv e-prints](#), p. [arXiv:2403.16471](#)
- Gandolfi S., Carlson J., Reddy S., 2012, *Phys. Rev. C*, **85**, 032801
- Garcia F., Chambers F. R. N., Watts A. L., 2019, *Phys. Rev. Fluids*, **4**, 074802
- Gendreau K. C., et al., 2016, in den Herder J.-W. A., Takahashi T., Bautz M., eds, *Society of Photo-Optical Instrumentation Engineers (SPIE) Conference Series Vol. 9905, Space Telescopes and Instrumentation 2016: Ultraviolet to Gamma Ray*, p. 99051H, doi:[10.1117/12.2231304](#)
- Goodwin A. J., Heger A., Chambers F. R. N., Watts A. L., Cavecchi Y., 2021, *MNRAS*, **505**, 5530
- Hansen C. J., van Horn H. M., 1975, *ApJ*, **195**, 735
- Hebeler K., 2021, *Phys. Rept.*, **890**, 1
- Heyl J. S., 2004, *ApJ*, **600**, 939
- Huth S., et al., 2022, *Nature*, **606**, 276
- Jahoda K., Swank J. H., Giles A. B., Stark M. J., Strohmayer T., Zhang W., Morgan E. H., 1996, in Siegmund O. H., Gummie M. A., eds, *Society of Photo-Optical Instrumentation Engineers (SPIE) Conference Series Vol. 2808, EUV, X-Ray, and Gamma-Ray Instrumentation for Astronomy VII*, pp 59–70, doi:[10.1117/12.256034](#)
- Jie Li J., Sedrakian A., Alford M., 2024, [arXiv e-prints](#), p. [arXiv:2401.02198](#)
- Keek L., Heger A., 2016, *MNRAS*, **456**, L11
- Kini Y., et al., 2023, *MNRAS*, **522**, 3389
- Kini Y., et al., 2024a, Pulse Profile Modelling of Thermonuclear Burst Oscillations III: Constraining the properties of XTE J1814–338, doi:[10.5281/zenodo.8365643](#), [https://doi.org/10.5281/zenodo.8365643](#)
- Kini Y., et al., 2024b, *MNRAS*, **527**, 8118
- Krauss M. I., et al., 2005, *ApJ*, **627**, 910
- Lattimer J. M., 2012, *Ann. Rev. Nucl. Part. Sci.*, **62**, 485
- Leahy D. A., Morsink S. M., Chung Y.-Y., Chou Y., 2009, *ApJ*, **691**, 1235
- Lee U., 2004, *ApJ*, **600**, 914
- Lo K. H., Coleman Miller M., Bhattacharyya S., Lamb F. K., 2013, *ApJ*, **776**, 19
- Mahmoodifar S., Strohmayer T., 2016, *ApJ*, **818**, 93
- Miller M. C., Lamb F. K., 1998, *ApJ*, **499**, L37
- Miller M. C., Lamb F. K., 2015, *ApJ*, **808**, 31
- Miller M. C., et al., 2019, *ApJ*, **887**, L24
- Miller M. C., et al., 2021, *ApJ*, **918**, L28
- Molkov S. V., et al., 2024, [arXiv e-prints](#), p. [arXiv:2404.19709](#)
- Morsink S. M., Leahy D. A., Cadeau C., Braga J., 2007, *ApJ*, **663**, 1244
- Nättälä J., Pihajoki P., 2018, *A&A*, **615**, A50
- Nättälä J., Miller M. C., Steiner A. W., Kajava J. J. E., Suleimanov V. F., Poutanen J., 2017, *A&A*, **608**, A31
- Oertel M., Hempel M., Klähn T., Typel S., 2017, *Rev. Mod. Phys.*, **89**, 015007
- Page D., 1995, *ApJ*, **442**, 273
- Papitto A., di Salvo T., Burderi L., Menna M. T., Lavagetto G., Riggio A., 2007, *MNRAS*, **375**, 971
- Patruno A., Watts A. L., 2021, in Belloni T. M., Méndez M., Zhang C., eds, *Astrophysics and Space Science Library Vol. 461, Timing Neutron Stars: Pulsations, Oscillations and Explosions*, pp 143–208 ([arXiv:1206.2727](#)), doi:[10.1007/978-3-662-62110-3\\_4](#)
- Pechenick K. R., Ftaclas C., Cohen J. M., 1983, *ApJ*, **274**, 846
- Piro A. L., Bildsten L., 2005, *ApJ*, **629**, 438
- Poutanen J., Beloborodov A. M., 2006, *MNRAS*, **373**, 836
- Poutanen J., Gierliński M., 2003, *MNRAS*, **343**, 1301
- Psaltis D., Özel F., Chakrabarty D., 2014, *ApJ*, **787**, 136
- Raaijmakers G., et al., 2021, *ApJ*, **918**, L29
- Ray P. S., et al., 2019, [arXiv e-prints](#), p. [arXiv:1903.03035](#)
- Riley T. E., 2019, PhD thesis, University of Amsterdam, [https://hdl.handle.net/11245.1/aa86fcf3-2437-4bc2-810e-cf9f30a98f7a](#)
- Riley T. E., et al., 2019, *ApJ*, **887**, L21
- Riley T. E., et al., 2021, *ApJ*, **918**, L27
- Riley T. E., et al., 2023, *Journal of Open Source Software*, **8**, 4977
- Salmi T., Nättälä J., Poutanen J., 2018, *A&A*, **618**, A161
- Salmi T., et al., 2022, *ApJ*, **941**, 150
- Salmi T., et al., 2023, *ApJ*, **956**, 138
- Scott D., 1992, *Multivariate Density Estimation: Theory, Practice, and Visualization*. A Wiley-interscience publication, Wiley, [https://books.google.nl/books?id=7crCUS\\_F2ocC](#)
- Spitkovsky A., Levin Y., Ushomirsky G., 2002, *ApJ*, **566**, 1018
- Stevens A. L., Fiege J. D., Leahy D. A., Morsink S. M., 2016, *ApJ*, **833**, 244
- Strohmayer T. E., Zhang W., Swank J. H., Smale A., Titarchuk L., Day C., Lee U., 1996, *ApJ*, **469**, L9
- Strohmayer T. E., Markwardt C. B., Swank J. H., in 't Zand J., 2003, *ApJ*, **596**, L67
- Suleimanov V., Poutanen J., Werner K., 2012, *A&A*, **545**, A120
- Tolos L., Fabbietti L., 2020, *Prog. Part. Nucl. Phys.*, **112**, 103770
- Vinciguerra S., Salmi T., Watts A. L., Choudhury D., Kini Y., Riley T. E., 2023, *ApJ*, **959**, 55
- Vinciguerra S., et al., 2024, *ApJ*, **961**, 62
- Virtanen P., et al., 2020, *Nature Methods*, **17**, 261
- Wang L., Steeghs D., Casares J., Charles P. A., Muñoz-Darias T., Marsh T. R., Hynes R. I., O'Brien K., 2017, *MNRAS*, **466**, 2261
- Watts A. L., Strohmayer T. E., Markwardt C. B., 2005, *ApJ*, **634**, 547
- Watts A. L., Patruno A., van der Klis M., 2008, *ApJ*, **688**, L37
- Watts A. L., et al., 2019, *Science China Physics, Mechanics, and Astronomy*, **62**, 29503
- Weinberg N., Miller M. C., Lamb D. Q., 2001, *ApJ*, **546**, 1098
- Wilms J., Allen A., McCray R., 2000, *ApJ*, **542**, 914
- Worpel H., Galloway D. K., Price D. J., 2015, *ApJ*, **801**, 60
- Yang J., Piekarewicz J., 2020, *Ann. Rev. Nucl. Part. Sci.*, **70**, 21
- Zhang S., et al., 2019, *Science China Physics, Mechanics, and Astronomy*, **62**, 29502
- van Baal B. F. A., Chambers F. R. N., Watts A. L., 2020, *MNRAS*, **496**, 2098

## APPENDIX A: APPENDIX

In Table A1, we show the run time for each burst for the Bkg free and Bkg constrained cases.

In Figure A1, we show the distribution of the residuals for Burst 1 for Bkg free and Bkg constrained for all the segments. The residuals are the difference between the model counts (for the maximum likelihood solution) normalized by the model count counts in each instrument energy channel and phase bin. The distributions of the residuals for the remaining bursts are available on Zenodo (see Kini et al. 2024a). There is no deviation from the overall expected Gaussian distribution which could hint at a shortcoming of the single hot spot model.

Figure A2 shows the combined posteriors for each subset (M1 and M2), along with the entire set of bursts in the Bkg constrained case. Both the M1 and M2 bursts favor regions with low masses and radii. The combined posteriors using the entire set of bursts are predominantly influenced by the M2 subset, as it contains a higher number of bursts (21 compared to 5 in the M1 subset).

In Figure A3, we show the combined posterior distributions of mass, radius, distance, observer inclination, column density, and compactness for Bkg constrained case. The posteriors were obtained using different Multinest live points. Increasing the number of live points by a factor of 50 yields the same results.

In Table A2, we provide a summary of the Multinest settings utilized in each inference run for individual bursts, as well as for the combined burst run.

We have compiled in Table A3 the Maximum A Posteriori values corresponding to each mode discovered for the various choices of Multinest live points in the combined burst run.

Burst	CPU core-hour ( $\times 10^4$ )	
	Bkg free	Bkg constrained
1	2.19	9.79
2	5.01	24.29
3	6.57	36.42
4	9.97	16.76
5	5.60	15.39
6	4.37	11.72
7	12.63	34.42
8	7.01	10.59
9	5.25	23.71
10	10.93	24.43
11	10.84	10.73
12	10.40	11.36
13	9.38	13.10
14	10.49	3.61
15	10.88	11.54
16	7.08	20.63
17	7.56	24.56
18	10.05	11.26
19	6.37	15.87
20	8.67	12.11
21	8.73	40.19
22	12.75	42.69
23	25.35	<b>40.25</b>
24	9.91	14.81
25	0.76	8.04
26	9.68	6.51
27	9.09	17.16
Total	237.52	511.94

**Table A1.** Core-hours spent on runs for each burst. Burst 23 in the Bkg constrained case had to be stopped due to resource constraints, having already consumed  $40.25 \times 10^4$  core-hours.

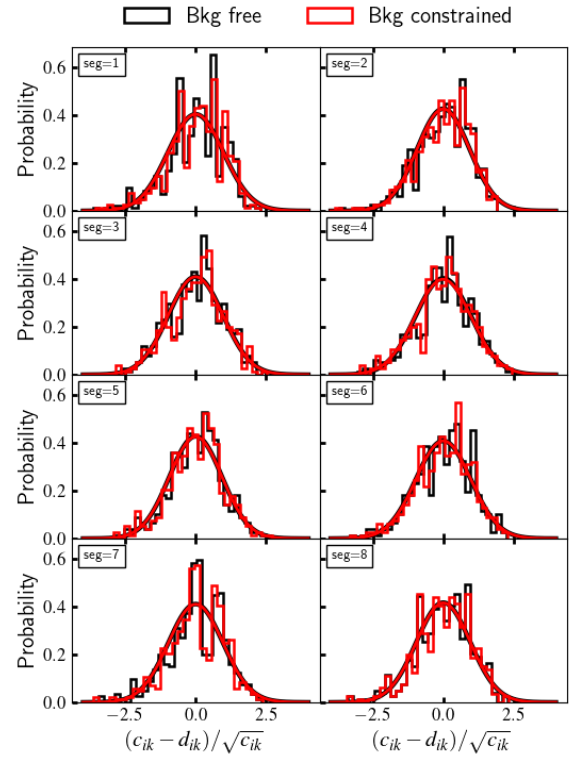


**Figure A1.** Histograms of the residuals for Burst 1 for Bkg free and Bkg constrained for all the segments. The residuals are the difference between the model counts (for the maximum likelihood solution) and the data counts, normalized by the model count counts in each instrument energy channel and phase bin. The solid lines are the Gaussian curves that fit best the histograms.

Variable	Value
multimodal	False
n_clustering_params	None
n_iter_before_update	None
n_live_points	2000
sampling_efficiency	0.1
const_efficiency_mode	False
evidence_tolerance	0.1
max_iter	-1

**Table A2.** Multinest settings used during the inference run of each burst as well as the combined burst runs, except for the combined burst we set multimodal :True



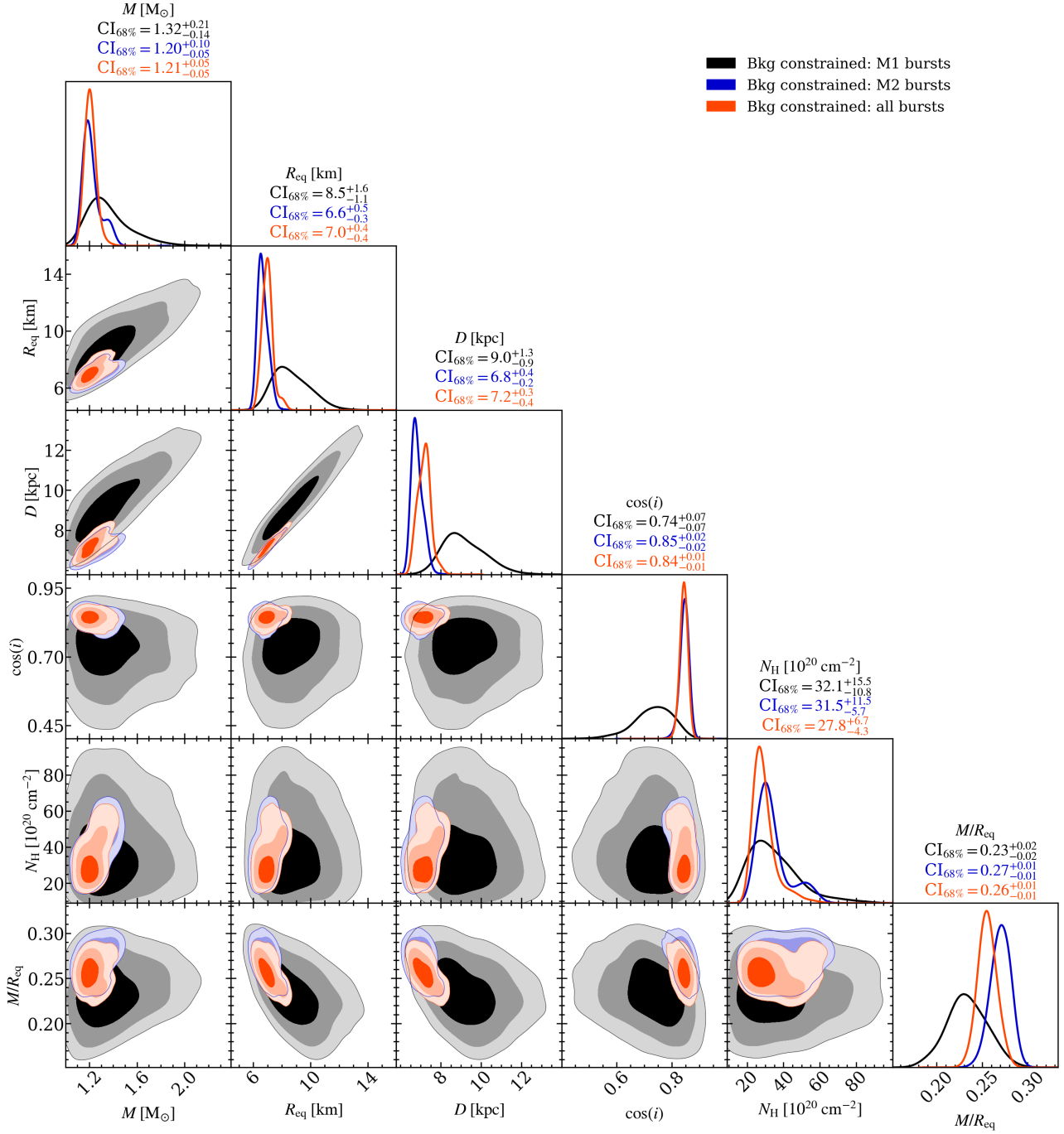


**Figure A2.** Combined posterior distributions of mass, radius, distance, observer inclination, column density, and compactness obtained using different Multinest live points. The two-dimensional posterior distributions are, from most opaque to least the 68%, 95%, and 99% posterior credible region.

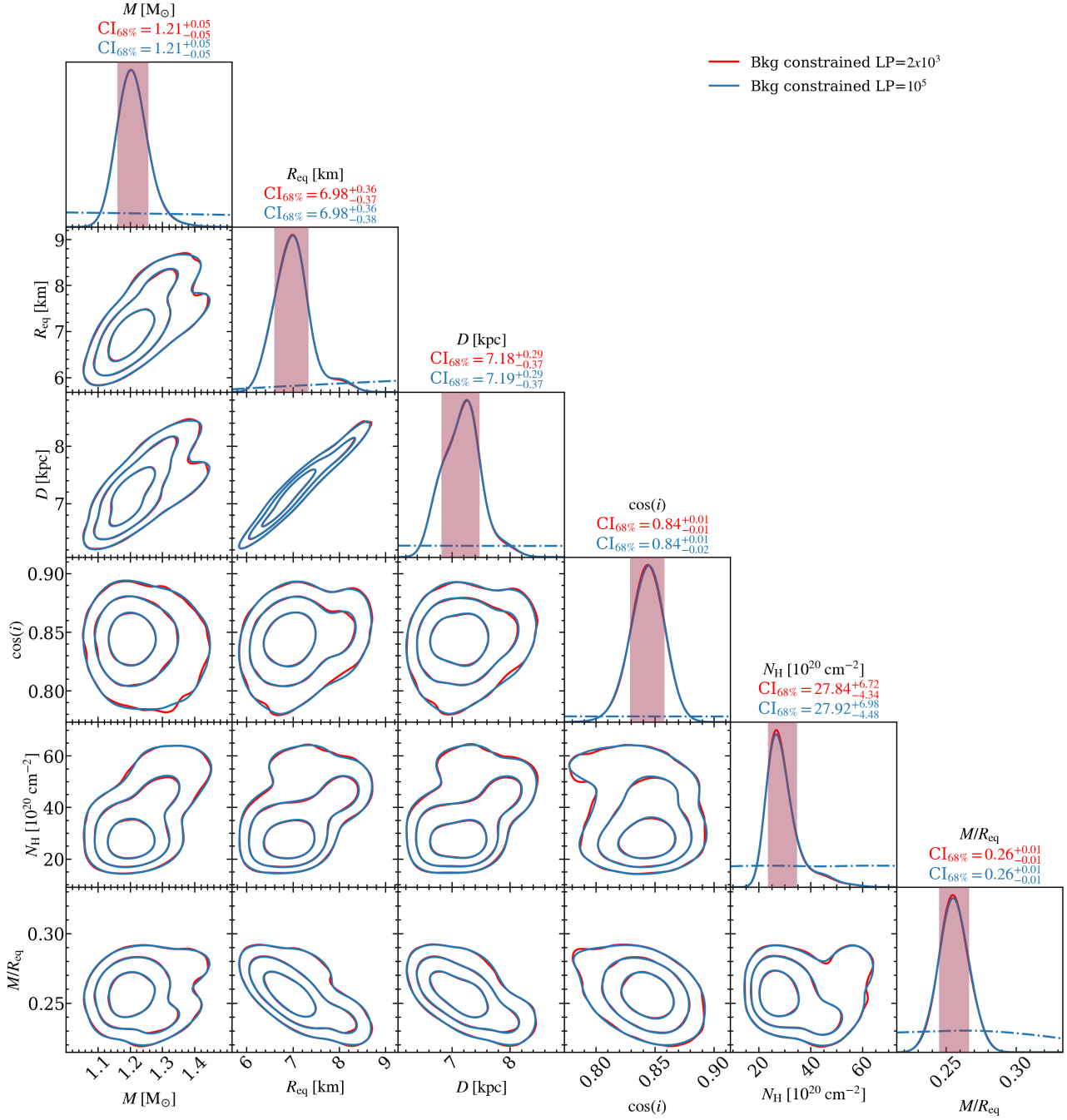


**Figure A3.** Combined posterior distributions of mass, radius, distance, observer inclination, column density, and compactness obtained using different Multinest live points. The two-dimensional contours are the 68%, 95%, and 99% posterior credible region. The solid (dash-dotted) lines along the diagonal represent the marginalized posterior (prior) distribution of each parameter. The vertical bands are the inferred 68% credible intervals.

Parameter		$M$ ( $M_{\odot}$ )	$R_{\text{eq}}$ (km)	$D$ (kpc)	$\cos(i)$	$N_H$ ( $10^{20}\text{cm}^{-2}$ )	Log-Evidence
$2 \times 10^3$ live points	Mode1	1.23	7.3	7.3	0.85	27.79	$-2256.57 \pm 0.09$
	Mode2	1.25	7.9	7.8	0.84	42.53	$-2308.18 \pm 0.94$
	Mode3	1.42	7.7	7.6	0.83	53.69	$-2314.70 \pm 0.70$
$10^5$ live points	Mode1	1.23	7.4	7.6	0.85	26.14	$-2258.19 \pm 0.12$
	Mode2	1.31	8.2	8.0	0.85	45.69	$-2309.25 \pm 0.13$
	Mode3	1.32	7.1	7.1	0.82	56.15	$-2314.86 \pm 0.10$
	Mode4	1.29	8.0	7.9	0.86	46.74	$-2336.74 \pm 0.56$
	Mode5	1.35	7.2	7.2	0.83	52.10	$-2342.11 \pm 0.43$
	Mode6	1.39	7.5	7.5	0.84	54.12	$-2351.93 \pm 0.68$
	Mode7	1.22	7.5	7.5	0.85	38.72	$-2355.02 \pm 0.14$
	Mode8	1.38	7.3	7.4	0.82	55.47	$-2357.56 \pm 0.86$
	Mode9	1.32	8.2	8.2	0.86	20.21	$-2454.75 \pm 0.87$

**Table A3.** Maximum A Posteriori values for each mode (ordered by evidence) for each `Multinest` live points choices.

This paper has been typeset from a  $\text{\LaTeX}$  file prepared by the author.